Observations of aerosol, cloud, turbulence, and radiation properties at the top of the marine boundary layer over the Eastern North Atlantic Ocean: The ACORES campaign

Holger Siebert, Kai-Erik Szodry, Ulrike Egerer, Birgit Wehner, Silvia Henning, Karine Chevalier, Janine Lückerath, Oliver Welz, Kay Weinhold, Felix Lauermann, et al.

BAMS Article

Observations of Aerosol, Cloud, Turbulence, and Radiation Properties at the Top of the Marine Boundary Layer over the Eastern North Atlantic Ocean

The ACORES Campaign

Holger Siebert, Kai-Erik Szodry, Ulrike Egerer, Birgit Wehner, Silvia Henning, Karine Chevalier, Janine Lückerath, Oliver Welz, Kay Weinhold, Felix Lauermann, Matthias Gottschalk, André Ehrlich, Manfred Wendisch, Paulo Fialho, Greg Roberts, Nithin Allwayin, Simeon Schum, Raymond A. Shaw, Claudio Mazzoleni, Lynn Mazzoleni, Jakub L. Nowak, Szymon P. Malinowski, Katarzyna Karpinska, Wojciech Kumala, Dominika Czyzewska, Edward P. Luke, Pavlos Kollias, Robert Wood, and Juan Pedro Mellado

ABSTRACT: We report on the Azores Stratocumulus Measurements of Radiation, Turbulence and Aerosols (ACORES) campaign, which took place around Graciosa and Pico Islands/Azores in July 2017. The main objective was to investigate the vertical distribution of aerosol particles, stratocumulus microphysical and radiative properties, and turbulence parameters in the eastern North Atlantic. The vertical exchange of mass, momentum, and energy between the free troposphere (FT) and the cloudy marine boundary layer (MBL) was explored over a range of scales from submeters to kilometers. To cover these spatial scales with appropriate measurements, helicopter-borne observations with unprecedented high resolution were realized using the Airborne Cloud Turbulence Observation System (ACTOS) and Spectral Modular Airborne Radiation Measurement System–Helicopter-Borne Observations (SMART-HELIOS) instrumental payloads. The helicopter-borne observations were combined with ground-based aerosol measurements collected at two continuously running field stations on Pico Mountain (2,225 m above sea level, in the FT), and at the Atmospheric Radiation Measurement (ARM) station on Graciosa (at sea level). First findings from the ACORES observations we are discussing in the paper are as follows: (i) we have observed a high variability of the turbulent cloud-top structure on horizontal scales below 100 m with local temperature gradients of up to 4 K over less than 1 m vertical distance, (ii) we have collected strictly collocated radiation measurements supporting the relevance of small-scale processes by revealing significant inhomogeneities in cloud-top brightness temperature to scales well below 100 m, and (iii) we have concluded that aerosol properties are completely different in the MBL and FT with often-complex stratification and frequently observed burst-like new particle formation.

Keywords: Aerosols; Cloud radiative effects; Small scale processes; Aircraft observations

https://doi.org/10.1175/BAMS-D-19-0191.1
Corresponding author: Holger Siebert, siebert@tropos.de
In final form 8 June 2020

AFFILIATIONS: Siebert, Szodry, Egerer, Wehner, Henning, Chevalier, Lückerath, Welz, and Weinhold—Leibniz Institute for Tropospheric Research (TROPOS), Leipzig, Germany; **Lauermann, Gottschalk, Ehrlich, and Wendisch**—Leipzig Institute for Meteorology, University of Leipzig, Leipzig, Germany; **Fialho**—Research Institute of Volcanology and Evaluation (IVAR), University of Azores, Ponta Delgada, Portugal; **Roberts**—Centre National de Recherches Météorologiques (CNRM), Université de Toulouse, Météo-France, CNRS, Toulouse, France, and Scripps Institution of Oceanography, University of California, San Diego, La Jolla, California; **Allwayin, Schum, Shaw, C. Mazzoleni, and L. Mazzoleni**—Michigan Technological University, Houghton, Michigan; **Nowak, Malinowski, Karpinska, and Kumala**—Faculty of Physics, University of Warsaw, Warsaw, Poland; **Czyzewska**—Faculty of Physics, University of Warsaw, Warsaw, Poland, and European Organisation for the Exploitation of Meteorological Satellites, Darmstadt, Germany; **Luke**—Brookhaven National Laboratory, Upton, New York; **Kollias**—Stony Brook University, State University of New York, Stony Brook, New York; **Wood**—University of Seattle, Seattle, Washington; **Mellado**—Universitat Politècnica de Catalunya, Barcelona, Spain

Stratocumulus (Sc) clouds are quite persistent and widespread over the globe, covering on average about 20% of Earth's surface (Wood 2012). Stratocumulus coverage plays a key role in maintaining the turbulent and radiative energy balance of the Sc-topped boundary layer (STBL). Turbulent and radiative energy fluxes at the cloud top are particularly important in this regard. The cloud-top region is one of the most important part of the STBL because the downward entrainment of potentially warm and dry air from the free troposphere (FT) into the cloud and subsequent mixing influences the whole cloud layer and is, therefore, crucial for the entire cloud life cycle. Comprehensive field campaigns to study the evolution of Sc have been performed focusing on larger scales (e.g., Lenschow et al. 1988; Stevens et al. 2003), but also looking at the small-scale features of the entrainment layer (Katzwinkel et al. 2012; Malinowski et al. 2013; Gerber et al. 2013).

Closely connected to the general atmospheric stratification is the spatial distribution of aerosol particles (Kanitz et al. 2013). Aerosol particles are eminently linked to the evolution of Sc, as they may serve as cloud condensation nuclei (CCN). In addition, Sc is also a likely source of aerosol particles due to new particle formation close to their top layer (Keil and Wendisch 2001; Wehner et al. 2015; Williamson et al. 2019), which may influence aerosol particle (N_p) and cloud droplet (N_d) number concentrations. Furthermore, long-range transport of aerosol particles plays an important role in the chemical composition (Schum et al. 2018; Dzepina et al. 2015), morphology (China et al. 2015, 2017), and vertical distribution of aerosol particles. Due to the different sources and sinks of aerosol particles, and the history of vertical motions and forcings, the spatial aerosol distribution is often characterized by complex and thin layers, which are closely connected to the structure of marine boundary layer (MBL) and the presence of decoupled layers at multiple levels. This holds true for both, cloudy and cloudless situations.

Considerable efforts have been spent to investigate the interplay of Sc with the aerosol-laden MBL and FT. The mass and energy (momentum and heat) exchange between the Sc layer and the FT takes place in the entrainment interfacial layer (EIL), which often extends only a few tens of meters in the vertical (Caughey et al. 1982). The specific characteristics of the EIL are fundamental for the exchange process. Wood (2012) pointed out that

> The nature of the EIL, particularly the strength of the gradients in buoyancy and horizontal winds, determines cloud-top entrainment (Wang and Albrecht 1994; Gerber et al. 2005; de Roode and Wang 2007). High temporal resolution and *collocated* measurements of liquid water, temperature, inactive tracers, humidity and turbulence, preferably from a slow-moving or stationary platform [e.g., the Airborne Cloud Turbulence

Observation System (ACTOS) helicopter platform; Siebert et al. (2006)], will be required to fully characterize and understand the EIL and how it affects entrainment.

This statement is a major motivation for the Azores Stratocumulus Measurements of Radiation, Turbulence and Aerosols (ACORES) project. Fundamental questions about the structure of the EIL, such as "How anisotropic is turbulence in the inversion due to shear and static stability, and how important is this anisotropy for entrainment and microphysical properties?" will be addressed.

Furthermore, the ACORES project is designed to answer the question of how the MBL and FT is stratified in terms of aerosol particles under cloudy and cloudless conditions. This includes investigations of new-particle formation, long-range transport of aerosol particles, and aerosol–cloud interaction.

This paper will introduce the ACORES project in terms of observation strategy, instrumentation, observed weather conditions, and it provides preliminary results in terms of selected highlights.

Observation strategy

The archipelago of the Azores (39°N, 28°W) is located about 1,200 km west of Portugal. It is an area representative for the eastern North Atlantic undisturbed by local pollution. Depending on the synoptical situation, this area can be considered as subtropical or midlatitudinal. Several observational campaigns, such as the Atlantic Stratocumulus Transition Experiment (ASTEX), took place in this region to study Sc and aerosol properties (Albrecht et al. 1995). The Clouds, Aerosol, and Precipitation in the Marine Boundary Layer (CAP-MBL) project (Wood et al. 2015; Rémillard et al. 2012) performed long-term measurements using the Atmospheric Radiation Measurement (ARM) Mobile Facility which is known as the eastern North Atlantic (ENA) ARM site (Mather and Voyles 2013).

The measurements of the ACORES project were collected by the ACTOS and the Spectral Modular Airborne Radiation Measurement System–Helicopter-Borne Observations (SMART-HELIOS). Both instrumental payloads were simultaneously carried by a helicopter as external cargo. The helicopter and the instrumental payload were deployed at the airport of Graciosa during July 2017. The helicopter-borne instrumentation allowed vertically resolved observations from ground up to about 3-km altitude covering the entire (cloudy) MBL and the lower part of the FT. However, these observations cover short periods of about two hours only, and therefore, are representative for a relatively limited region and time period. To overcome this restriction, two continuously operating ground-based measurement stations complemented the airborne sampling: (i) the permanent ENA site located at sea level at the airport of Graciosa Island and, (ii) a smaller station called Observatório da Montanha do Pico (OMP) on top of Mount Pico at a height above ground level of 2,225 m, representing the conditions in the FT (Kleissl et al. 2007). The general measurement area and strategy with the helicopter-borne observations and ground-based stations is illustrated in Fig. 1. The aerial picture of Graciosa taken during a measurement flight nicely illustrates the close collocation between the airport (and the ENA site) and the operational area for the helicopter off the coast.

A schematic of ACTOS and SMART-HELIOS is given in Fig. 2, together with selected processes and mean conditions of the cloudy MBL. Whereas ACTOS is measuring cloud properties in situ, SMART-HELIOS is well above the cloud layer measuring remotely cloud-top properties.

Observing platforms and instrumentation

ACTOS and SMART-HELIOS are instrument payloads carried by a 170-m-long tether fixed to a helicopter as two separate external cargo; they are mounted about 170 m (ACTOS) and 20 m (SMART-HELIOS) below the helicopter. During the ACORES campaign, ACTOS and

SMART-HELIOS were carried by a twin-engine Airbus helicopter of type BO-105 equipped for offshore flights. The endurance is about 2 h (without safety time) with a maximum ceiling of 3,000 m. Most of the flights have been performed offshore north of Graciosa in a maximum distance to the airport of 20 km. A typical true airspeed (TAS) of 20 m s^{-1} allows for high spatial resolution of the measurements at a given high sampling rate. Compared to fast-flying research aircraft, technical issues typically disturbing airborne measurements are negligible, e.g., particle inlet problems or issues caused by the adiabatic heating of (wetted) sensors (Wendisch and Brenguier 2013). See the sidebar for a discussion about profiling with helicopter and small aircraft.

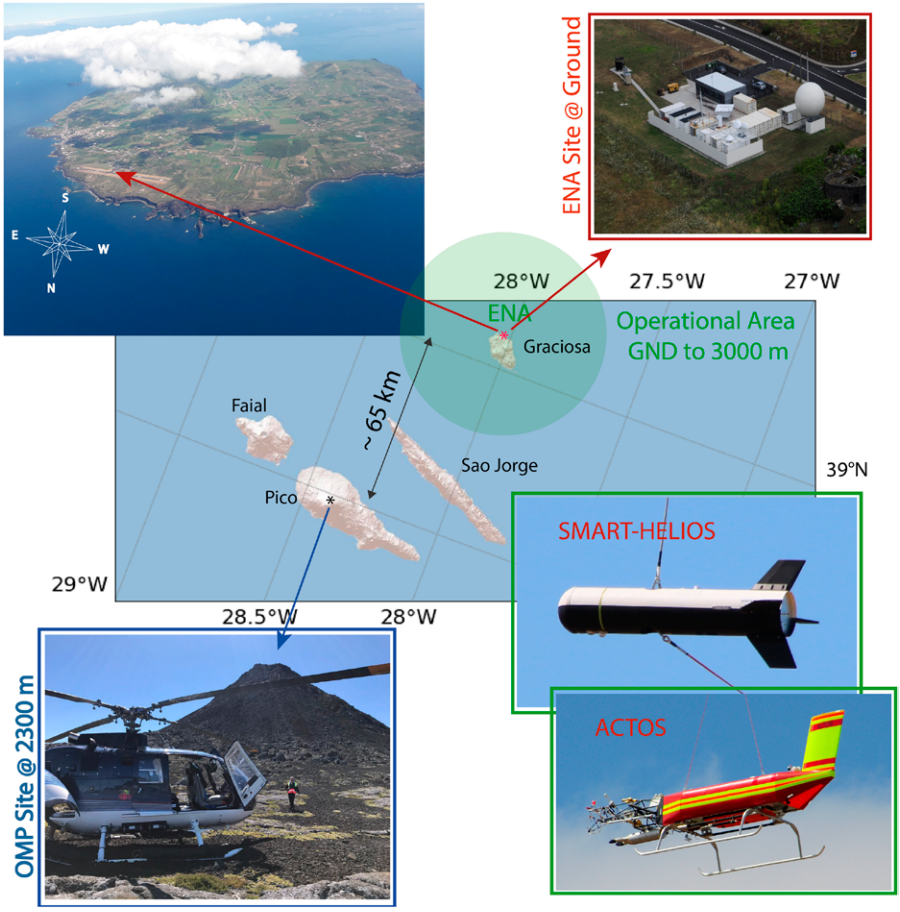

Fig. 1. Map with the three major components of the ACORES campaign: continuously running ENA and OMP stations, and the helicopter-borne ACTOS and SMART-HELIOS. The red arrow in the aerial photo of the island of Graciosa shows the location of the airport and ENA.

The 170-m-long tether allows sampling with ACTOS inside the Sc, whereas SMART-HELIOS and the helicopter can safely operate above the cloud under visible flight rules. This setup allows for an almost perfect spatial collocation of in situ (ACTOS) and remote sensing (SMART-HELIOS) observations (cf. Fig. 2).

Helicopter-borne: ACTOS. ACTOS is an autonomous helicopter-borne payload with a maximum total weight of 250 kg and an overall length of 5.5 m. The general concept of ACTOS has been introduced in Siebert et al. (2006) and a photo is shown in Fig. 1.

ACTOS is equipped with various sensors for high-resolution sampling of standard meteorological parameters. The three-dimensional wind vector as measured by an ultrasonic anemometer–thermometer in combination with a high-accuracy motion

Profiling with aircraft and helicopter

A critical point, which should be considered when observing cloud-top layers with fast-flying aircraft, is the issue of averaging over several eddies during profiling. All airborne profiles are slanted and the steepness of the profiles depend on the ratio of TAS and climb rate w_A. For a given vertical extent of the EIL δ_z, the horizontal flight path L is given by $L = (\mathrm{TAS}/w_a)\,\delta_z$. For smaller research aircraft, a TAS of 50 m s^{-1} and a climb rates of $w_a \sim 1.5$ m s^{-1} (Malinowski et al. 2013; Gerber et al. 2016) is typical. The ratio TAS/w_a is comparable to fast-flying research aircraft with a TAS ~ 150 m s^{-1} combined with climb rates of $w_a \sim 5$ m s^{-1} (Desai et al. 2019). For a typical thickness of an EIL of $\delta_z = 100$ m, this results in a flight path of $L = 3$ km, corresponding to 30 large-eddy length scales assuming that the largest eddies $\propto \delta_z$. In contrast, ACTOS observations of this study have typically values of $w_a \sim 5$ m s^{-1} (and 2 m s^{-1} for descents) combined with TAS ~ 20 m s^{-1} yielding $L = 400$ m (1,000 m for descents) and resulting in much steeper profiles with averaging over only 4–10 individual eddies. This distinction between aircraft-derived profiles that are heavily averaged and helicopter-derived profiles that are closer to a single realization, should be kept in mind when interpreting the results.

package (inertial navigation system and GPS) in order to transform the measured wind vector to an Earth-fixed system. Fine-wire sensors, such as one-component hot wires (Siebert et al. 2007) for turbulence and cold wires for temperature observations [ultrafast thermometer (UFT) family; Haman et al. 1997; Kumala et al. 2013], provide high-resolution measurements of the small-scale (cloud) turbulence with centimeter resolution. Humidity fluctuations are observed by an infrared absorption hygrometer (open-path LiCor 7500; Lampert et al. 2018) with at least submeter resolution.

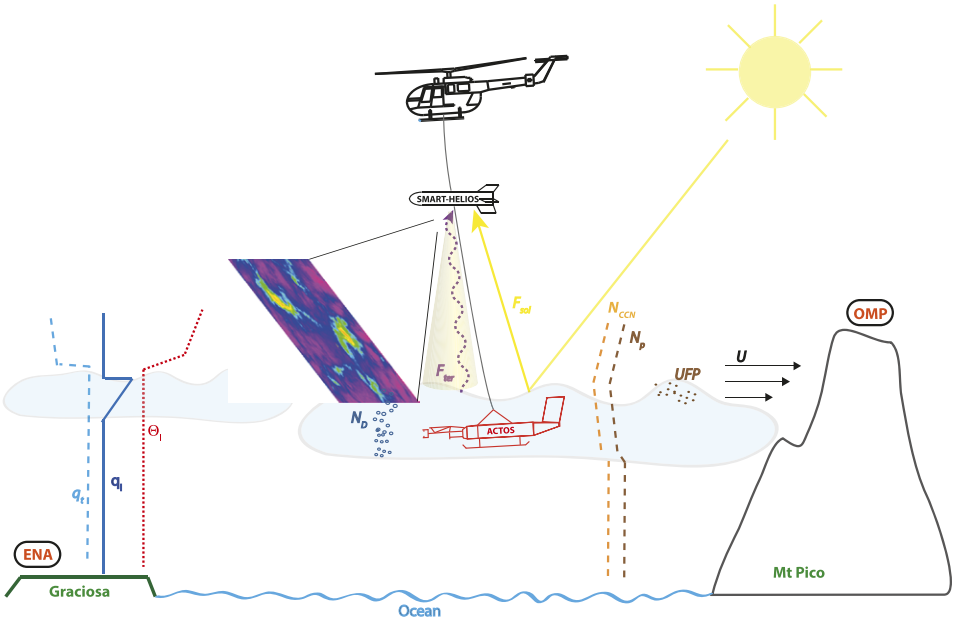

Fig. 2. Cartoon of the main processes in a STBL and the sampling strategy with the two helicopter-borne payloads, ACTOS and SMART–HELIOS. The ground-based ENA (surface) and OMP (free troposphere) sites are also indicated. Typical mean profiles are shown for total water mixing ratio q_t, liquid water mixing ratio q_l, liquid water potential temperature θ_l, horizontal wind speed U, aerosol particle (N_p), cloud droplet (N_D), and CCN (N_{CCN}) concentrations, and solar and terrestrial irradiance (F_{sol} and F_{ter}). Ultrafine particles (UFP) are frequently observed around cloud top.

The high-resolution measurements are combined with precise sensors, such as a carefully calibrated PT100 and a small dewpoint mirror, with comparably slow response times (~1 s), by complementary filtering to obtain fast but also precise and long-term stable signals (Wendisch and Brenguier 2013).

Bulk cloud parameters such as liquid water content (LWC), particle surface area (PSA), and effective radius (r_{eff}) are measured with the particle volume monitor (PVM; Gerber et al. 1994; Wendisch et al. 2002). Cloud parameters based on single droplet measurements are additionally measured with the cloud droplet probe 2 (CDP-2; Lance et al. 2010).

Aerosol particle number concentration and size distribution ranging from 8-nm to 2-μm particle diameter are measured by a mobility particle size spectrometer (MPSS) and optical particle sizing system (OPSS) as described in Wehner et al. (2010). A lightweight cloud condensation nuclei counter (miniCCNC; Roberts and Nenes 2005) has been additionally integrated on ACTOS in order to measure CCN number concentration N_{CCN} at 0.2% supersaturation.

A set of upward- and downward-oriented pyranometer and pyrgeometer (same type as integrated on SMART-HELIOS; see next section) provide upward and downward solar and thermal infrared irradiance.

Online (live) monitoring of the ACTOS measurements is possible for the two scientists on board the helicopter during flight. The battery and fuel capacities allow for unattended measurements with instrumentation installed on ACTOS of about two hours. An overview of ACTOS's instrumentation during ACORES including specifications is provided in Table 1.

Helicopter-borne: SMART-HELIOS. Solar and terrestrial radiation (spectral and broadband) below, above, and within the Sc are measured by SMART-HELIOS with a combination of different sensors (see Table 2). Compared to a previous version described by Werner et al. (2013,

Table 1. Overview of all parameters measured on ACTOS.

Parameter measured on ACTOS	Symbol	Sensor and type	Resolution
Wind vector in sensor-fixed system	$\mathbf{U}_S = (u_S, v_S, w_S)$	3D ultrasonic anemometer (Solent HS)	100 Hz
Attitude and motion	$\Psi, \Phi, \Theta, \mathbf{U}_A$	Inertial navigation unit (IMU)	100 Hz
Position	φ, λ, z	GPS	1 Hz
Wind vector in Earth-fixed system	$\mathbf{U}_E = (u_E, v_E, w_E)$	Sonic, attitude, and motion	100 Hz
Small-scale turbulence	u	Hot-wire anemometer	2,000 Hz
Liquid water content	LWC	Particle volume monitor (PVM-100 A)	1,000 Hz
Particle surface area	PSA		1,000 Hz
Cloud droplet diameter	d_d	Cloud droplet probe (CDP-2)	1 Hz
Number concentration	N_d		
Water vapor density	ρ_v	Fast dewpoint mirror	1 Hz
		IR-absorption hygrometer (LI7500)	20 Hz
Static pressure	p	Capacitive sensor (Barocap, PTB220)	10 Hz
Static temperature	T	PT100 (Rosemount Type 139)	1 Hz
		Ultrafast thermometer (UFT)	1–4 kHz
Sonic temperature	T_s	Ultrasonic thermometer	100 Hz
Total particle number concentration (>8 nm)	N_p	Condensation particle counter (CPC)	1 Hz
Total particle number concentration (>10 nm)	$N_{p,\mathrm{Fast}}$	Fast-mixing-type CPC	10 Hz
CCN number concentration at $S = 0.2\%$	N_{CCN}	Mini cloud condensation nuclei counter	1 Hz
Particle number size distribution (8–350 nm)	PNSD	Scanning mobility particle sizer (SMPS)	120 s
Particle number size distribution (350–2,500 nm)		Optical particle counter (OPC)	1 Hz
Particle absorption coefficient (450, 525, 624 nm)		Absorption photometer (STAP)	1 Hz
Broadband solar irradiance (0.2–3.6 μm)	$F_{\mathrm{sol}}^{\uparrow}, F_{\mathrm{sol}}^{\downarrow}$	Up- and downward pyranometer (CMP22)	100 Hz
Broadband terrestrial irradiance (4.5–42 μm)	$F_{\mathrm{ter}}^{\uparrow}, F_{\mathrm{ter}}^{\downarrow}$	Up- and downward pyrgeometer (CGR4)	100 Hz

2014), SMART-HELIOS was extended by a set of two CMP22 pyranometers and two CGR4 pyrgeometers measuring the upward and downward broadband solar and terrestrial irradiances. The two CMP22 cover the solar spectral wavelength range between 0.2 and 3.6 μm. The CGR4 are sensitive to terrestrial radiation in the wavelength range of 4.5–42 μm. The sensors are calibrated as secondary standards with uncertainties of 0.8% for the solar irradiance and 4% for the terrestrial irradiance. The data acquisition is operated with a sampling frequency of 20 Hz; the data are corrected for the sensor inertia (Ehrlich and Wendisch 2015). The downward solar irradiance is corrected for misalignments of SMART-HELIOS with respect to the horizontal plane using the approach proposed by Bannehr and Schwiesow (1993). The attitude of SMART-HELIOS is measured by an inertial measurement unit providing pitch, roll, and heading with a dynamic accuracy of ±2°. The impact of the helicopter on the downward measurements is minor for SMART-HELIOS being located 20 m below. Measurements with the direct sun shaded by the helicopter are filtered in the data analysis. Solar spectral nadir radiance $I_\lambda^{\uparrow}$ reflected by the clouds is measured by plane grating spectrometers covering the spectral range from 0.35 to 2.1 μm with a spectral resolution (full width at half maximum) of 2–10 nm (Werner et al. 2013).

Two camera systems are employed to characterize the horizontal structure of the cloud top. The thermal-infrared camera Xenics Gobi-640 GigE measures the emitted terrestrial radiation

in the wavelength range of 8–14 μm. The images provide a resolution of 640 pixel × 480 pixel within a field of view of 57.1° × 44.4°. For SMART-HELIOS, located 150 m above cloud top, this results in an image width of about 120 m and a pixel size of about 0.2 m. The sensor is calibrated in terms of brightness temperatures with a thermal resolution of 50 mK. Images of the solar radiation reflected by the clouds are obtained with a digital RGB camera every 10–15 s. The resolution of the images is 3,264 pixels × 2,448 pixels within a field of view of 50.1° × 38.3°.

To estimate the cloud-top altitude, a laser altimeter ILM-500-R was installed in a downward-looking direction. The laser module operates at a wavelength of 905 nm and detects the cloud top if sufficient liquid water is present. The uncertainty of cloud-top altitude is estimated to be 5 m. An overview of all sensors on SMART-HELIOS is given in Table 2.

Table 2. Overview of all parameters measured on SMART-HELIOS.

Parameter measured on SMART-HELIOS	Symbol	Sensor and type	Resolution
Broadband solar irradiance (0.2–3.6 μm)	$F_{sol}^{\uparrow}$, $F_{sol}^{\downarrow}$	Up- and downward pyranometer (CMP22)	20 Hz
Broadband terrestrial irradiance (4.5–42 μm)	$F_{ter}^{\uparrow}$, $F_{ter}^{\downarrow}$	Up- and downward pyrgeometer (CGR4)	20 Hz
Spectral nadir radiance (350–2,100 nm)	$I_{\lambda}^{\uparrow}$	Grating spectrometer (field of view 2°)	2–3 Hz
Brightness temperature (8–14 μm)		Thermal-IR camera (Gobi-640 GigE, 640 pixels × 480 pixels, FOV = 57°)	5 s
RGB images		Canon IXUS 80 IS, 3,264 pixels × 2,448 pixels, FOV = 50.1°	10–15 s
Cloud-top height	h_{ct}	Laser altimeter (ILM-500-R)	5 s
Attitude	Ψ, Φ, Θ	Attitude heading reference system (MicroStrain 3DM-GX3–25)	10 Hz
Position	φ, λ, z	GPS	1 Hz

Ground based: Aerosol observation sites. Two ground-based measurement stations were set up on the Azorean islands of Graciosa. Measurements on Graciosa were carried out at the ARM facility ENA, which has been operating as a permanent facility since 2013. The ENA observatory is located on the north of the island, close to the airport and the height is close to mean sea level. Predominant winds from north and west assure minimal island effects on the measurements performed at the ENA site (Dong et al. 2014). In addition to the continuous measurements at ENA, aerosol particle number size distributions and particle number concentrations down to 10 nm were measured during ACORES.

The second ground-based station was located at OMP, on top of the volcano Pico 2,225 m above sea level (Honrath et al. 2004). The OMP site can be assumed to be a station representative for the FT (Collaud Coen et al. 2018). The mountain peak is surrounded by a circular caldera with 20-m-high rock walls on the southwest side while a small volcanic cone (126 m tall), called "Piquinho," is situated in the southeast of the station. Wind measurements at the OMP are available but are influenced by the caldera walls and the Piquinho. The OMP performs measurements of meteorological parameters, trace gases, aerosol scattering and backscattering, and black carbon equivalent mass concentration. Samples for offline chemical and microscopy analysis are collected regularly. Aerosol particle number size distributions down to 10 nm were measured for the first time at the OMP during the ACORES campaign. Also, as part of the ACORES campaign, a CCN counter (CCNC) was operating at the OMP in July 2017.

Both ground-based stations were equipped with an MPSS, but the station in Graciosa had an additional CPC to measure the total number concentration. The MPSS setup and calibration followed the recommendations described by Wiedensohler et al. (2012). A complete list of all ground-based sensors is given in Table 3.

Table 3. Overview of all parameters measured additionally during the ACORES campaign at ENA and OMP.

Parameter measured at ENA			
Total particle number concentration (>10 nm)	N_p	CPC	1 Hz
Particle number size distribution (10–800 nm)	PNSD	SMPS	5 min
Particle number size distribution (>800 nm)	PNSD	Aerodynamic Particle Sizer (APS)	5 min
Parameter measured at PMO			
Particle number size distribution (10–800 nm)	PNSD	SMPS	5 min
Particle number size distribution (>800 nm)	PNSD	APS	5 min
CCN number concentration at $S = 0.2\%$	N_{CCN}	Mini cloud condensation nuclei counter	1 Hz

Synoptic conditions and data overview

Synoptic conditions. The synoptic situation on the Azores archipelago is, in general, mainly influenced by the location and strength of the Azores high pressure system. During the campaign, the high was pronounced and its center was located either west or north of the island. Occasionally, fronts passed the Azores. A time series of potential air temperature, absolute air humidity, and horizontal wind vector profiles measured by regular radiosonde launches at the ENA station is shown in Fig. 3. The profiles are shown for the typical altitude range of the helicopter operations (<2,500 m) and cover the entire ABL. Profiles of radar reflectivity of the Ka-band ARM zenith radar and estimated cloud-base height are shown in Fig. 4.

Based on the time series of the local weather conditions affecting the ABL, three periods of prevailing synoptic regimes were identified, which are summarized in Table 4. Maps of the mean surface pressure, surface wind vector, and potential temperature in 950-hPa pressure level are provided in Fig. 5 based on the fifth generation of the European Centre for Medium-Range Weather Forecasts (ECMWF) atmospheric reanalyses (ERA5) data

Table 4. Periods of ACORES defined from the synoptic weather conditions during the measurement period.

Period	Dates	Summary
I	1–11 Jul 2017	Azores high located west, stable conditions with northerly flow of dry and cold air, low cloud fraction with thin shallow convection, less precipitation, front passed on 7/8 Jul
II	12–19 Jul 2017	Azores high centered above, weak winds, warm and moist air mass, daily cycle of stronger shallow convection with frequent precipitation, fronts passed on 17 and 19 Jul
III	20–25 Jul 2017	Azores high located west, stable conditions with changing winds, dry and cold air mass, low cloud fraction with shallow convection, less precipitation, front passed on 23 Jul

(Hersbach et al., 2018a, b). The first synoptic period (2–11 July) was characterized by the lowest ABL temperatures of the entire campaign, associated with relatively dry air. This air mass prevailed due to a weak northerly flow and stable conditions at the northeasterly edge of the Azores high pressure system. In this period, cloud cover was low and dominated by thin shallow convection with little amount of precipitation (Fig. 4). On 3, 6, and 7 July, frontal systems passed the station leading to a temporal westerly flow associated with an increase in air temperature, humidity, and precipitation.

The second period (12–19 July) was affected by a weakening and shift of the Azores high pressure system. The center was located farther west while a tail of weak high pressure stretched in northeastward direction over the archipelago. During this time, an increase of air temperature and humidity within the entire ABL was observed. Supported by the weaker high pressure, convection amplified within this air mass and led to the development of thicker

Sc clouds that produced precipitation.

On 17 July, a front associated with a strong and quickly eastward-moving low pressure system north of the islands did pass Graciosa and affected the location of the Azores high. After a second frontal passage on 19 July, the stable conditions recovered with the center of the Azores high located west of the archipelago. This defined the start of the third synoptic period of the campaign (20–22 July). Similar to the first period, the ABL was dominated by colder, dry air with reduced cloud cover and less precipitation.

Based on the vertical temperature profiles obtained from the radiosondes, the temperature inversion was localized following the method applied by Kahl (1990) and Andreas et al. (2000). The temperature profiles and the location of the inversion layers are presented in Fig. 6c. Scanning the profile from the surface, the inversion base was identified where the first positive temperature gradient was observed. The altitude of the inversion top was then defined by the next altitude, where the temperature started to decrease. Repeating this analysis above the inversion top, a second inversion was identified in nine profiles. To remove weak inversions, which may be only measurement artifacts, inversions where none of the single 5-m layers showed a vertical temperature increase of more than 0.2 K $(5\ \mathrm{m})^{-1}$ were not counted. Similarly, inversion layers thinner than 30 m or with inversion-base height below 500 m were neglected. The resulting inversion strength, defined

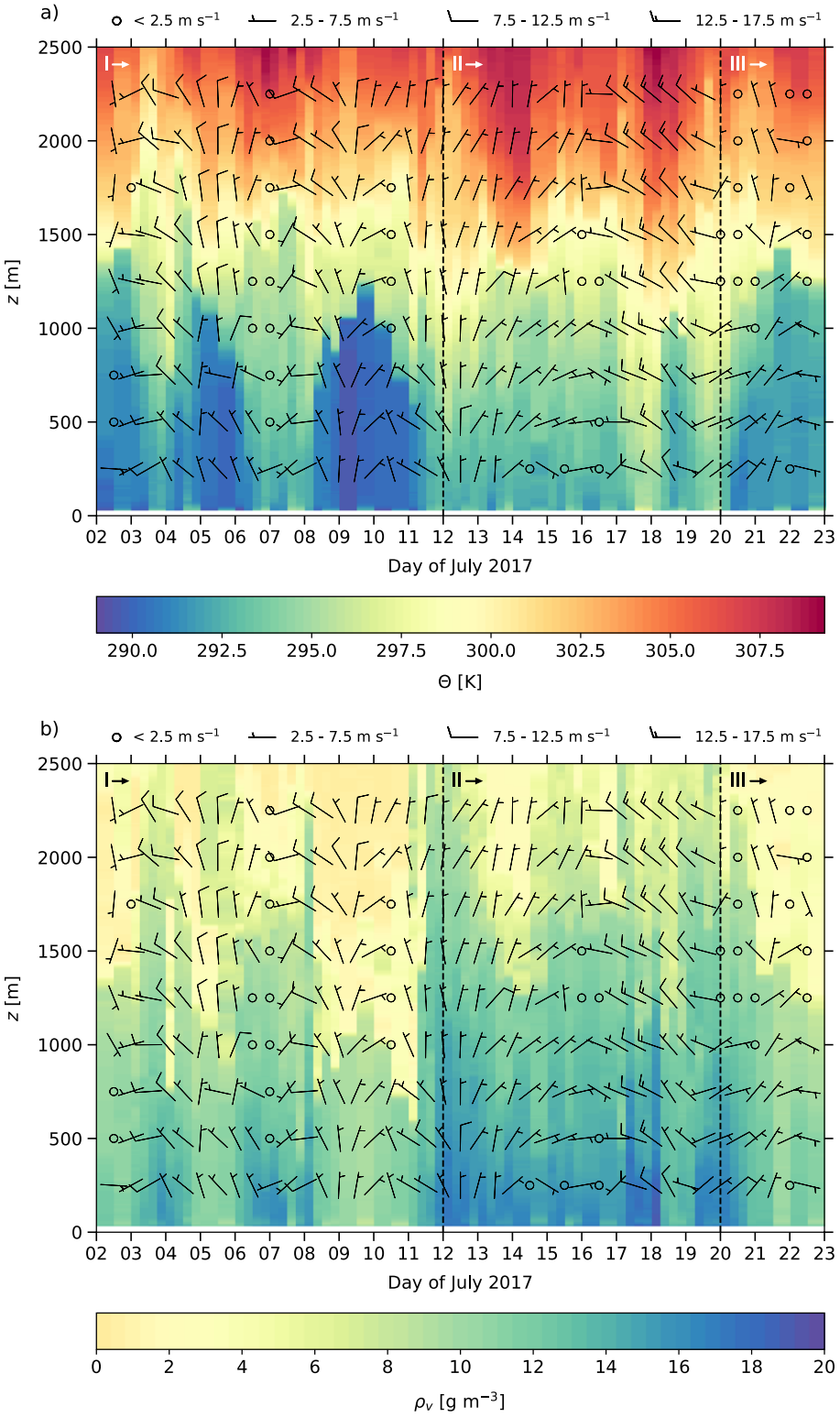

Fig. 3. Contour plots of the (a) potential temperature (Θ) and (b) water vapor density (ρ_v) profiles derived from regular radiosonde launches at ENA. The horizontal wind vector is indicated by wind barbs in both panels. The labels I, II, and III and the vertical dashed lines indicate the starts of the three synoptic periods of the ACORES campaign.

by the difference between minimum and maximum temperature below and above the inversion and the maximum temperature gradient within a 30-m vertical interval are shown in Figs. 6a and 6b, respectively. The ABL inversions are most pronounced in terms of frequency of occurrence and partly in terms of the inversion strength during the stable condition of periods 1 and 3. During passages of fronts and frequently during period 2, fewer inversions were identified. The inversion-top height varied between 500 and 2,000 m and follows the cloud geometry observed by the cloud radar (see Fig. 4). The inversion strength is highly variable with total temperature increases ranging between 0.5 and 5.5 K. In most of the inversions the major contribution of this temperature jump is observed within a single 30-m layer (cf. Figs. 6a,b). This indicated that the inversion strength strongly depends on the presence of a cloud layer, where strong radiative cooling at cloud top strengthens and sharpens the inversion layer.

Aerosol measurements at ENA and OMP. A characteristic bimodal shape of the aerosol particle number size distribution within the MBL was observed

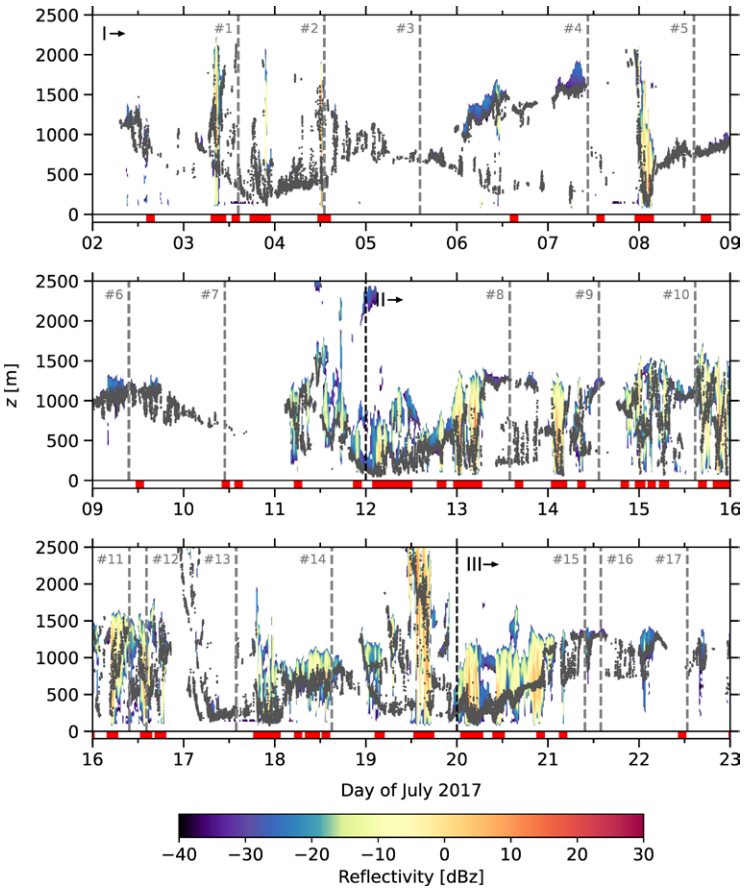

Fig. 4. Time series of radar reflectivity measured by the Ka-band ARM zenith radar at ENA during the period of ACORES in July 2017. Gray dots indicate the cloud-base height derived from ceilometer measurements. A rain flag (red bars) identified by a laser disdrometer is given below the radar profiles. The time of takeoff for the helicopter flights is indicated by the dashed gray lines. The labels I, II, and III and the dashed black lines indicate the starts of the three synoptic periods of the ACORES campaign.

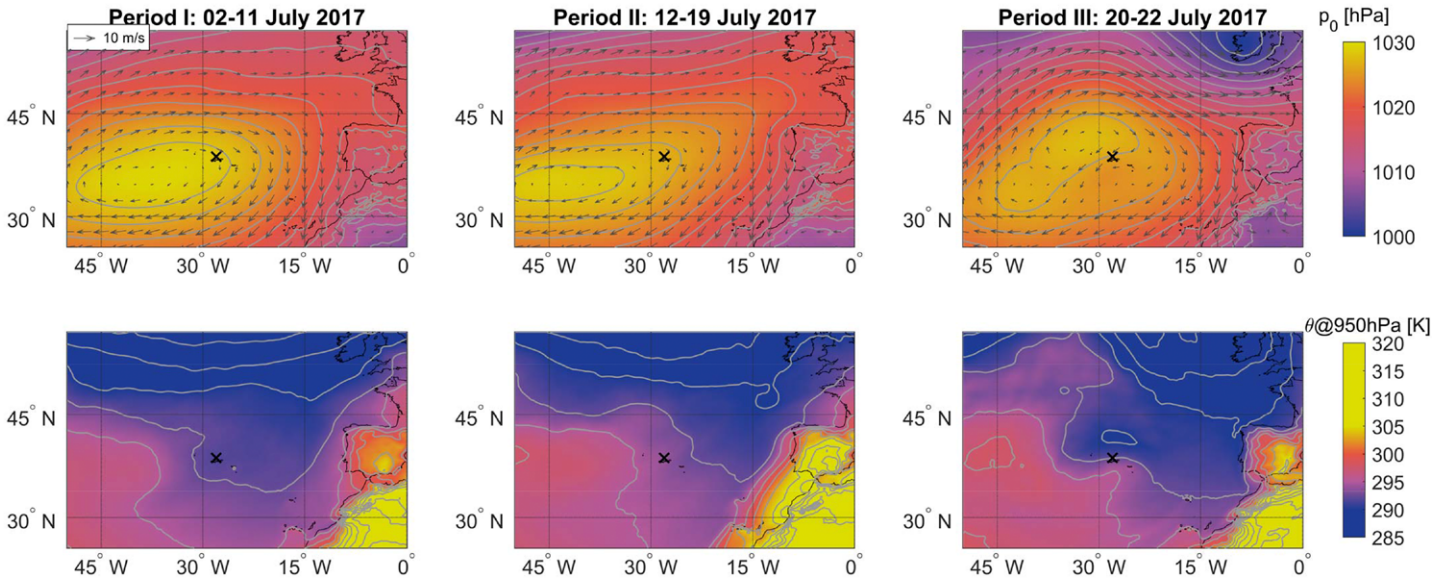

Fig. 5. Mean (top) surface pressure and wind vectors and (bottom) potential temperature at 950 hPa calculated from ERA5 for the three synoptic periods of the ACORES campaign.

throughout most of the measurement period at the ENA station, as seen in Fig. 7. The number concentration and mean diameters of aerosol particles in the Aitken and accumulation modes varied according to the airmass transport and meteorological conditions. A merge of Aitken and accumulation modes was observed at the ENA station on 10 July, when the Aitken mode particles grew continuously toward the accumulation mode. According to the meteorological conditions described in the "Helicopter-borne: ACTOS" section the second period is associated with high humidity and precipitation, and therefore, shows the lowest number concentration in the two modes compared to periods 1 and 3.

The proximity of the ENA station to the Graciosa airport affected the measured aerosol number concentrations. The airport received two flights per day, besides the ACTOS measurement flights, causing spikes in the aerosol number concentrations (see Fig. 7).

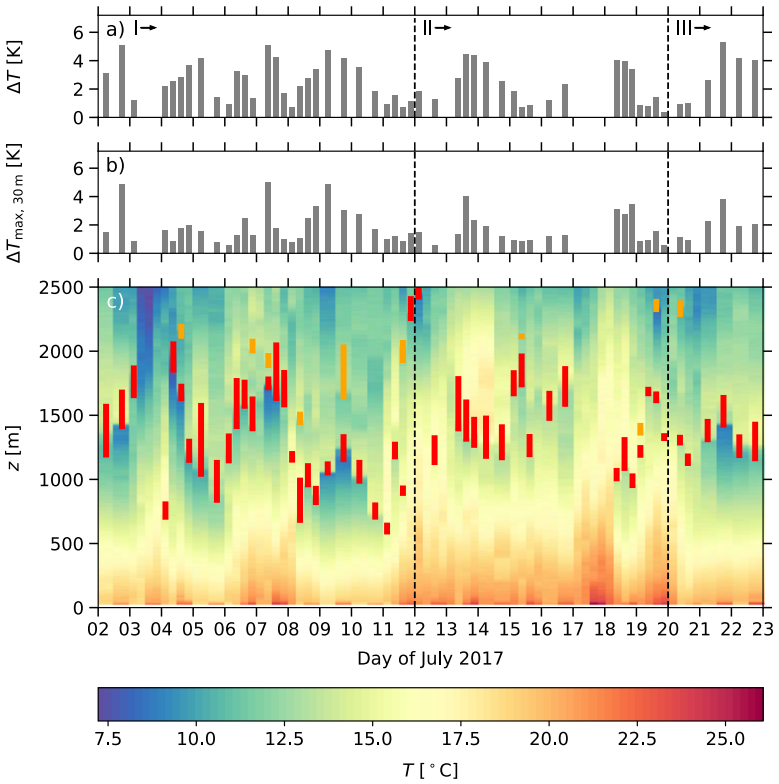

Fig. 6. (c) Time series of air temperature measured by radiosondes at ENA during the period of ACORES in July 2017. The height of identified temperature inversions with base heights larger than 500 m is indicated by the red (lowest inversion) and orange (higher inversions) bars. For each lowermost identified inversion, we also show (a) the total inversion strength and (b) the maximum temperature gradient observed within a 30-m vertical layer. The labels I, II, and III and the dashed black lines indicate the starts of the three synoptic periods of the ACORES campaign.

The measurements at OMP in the free troposphere, displayed in Fig. 8 show a different behavior. Most of the time one mode with a mean diameter in the Aitken size range dominated the particle number size distribution. On 5 July, an increase of accumulation-mode particles due to the long-range transport of air masses from North America resulted in a bimodal aerosol particle number size distribution in the free troposphere. This fits well with the ACTOS measurements as shown in a case study (later shown in Fig. 12). An aerosol scavenging event was observed at the OMP during the night of the 7–8 July and an increase in number concentration of aerosol particles up to 30 nm was recorded. The last week of measurements revealed four aerosol scavenging events and the increase of small particle concentrations, with diameters up to 30 nm on 20 July. Obviously, also the ratio between the number concentration of CCN and all aerosol particles is variable.

Overview of helicopter flights and sampling strategy. For the period between 3 and 22 July 2017, 17 research flights with ACTOS and SMART-HELIOS were performed in addition to the continuously running aerosol observations at OMP and ENA. Table 5 provides an overview of all flights. The flights are sorted in terms of the three different synoptic periods.

Each helicopter flight starts with a vertical profile from about 100 m above sea level up to about 2,000 m under cloudless conditions in order to obtain an overview about thermal stratification and aerosol layering directly followed by a 10-km-long horizontal leg, which allows for at least two scans of an aerosol size distribution in the FT.

The subsequent flight pattern depends on local cloud conditions but usually consists of legs in a constant height in and above the Sc layer combined with several porpoise dives of

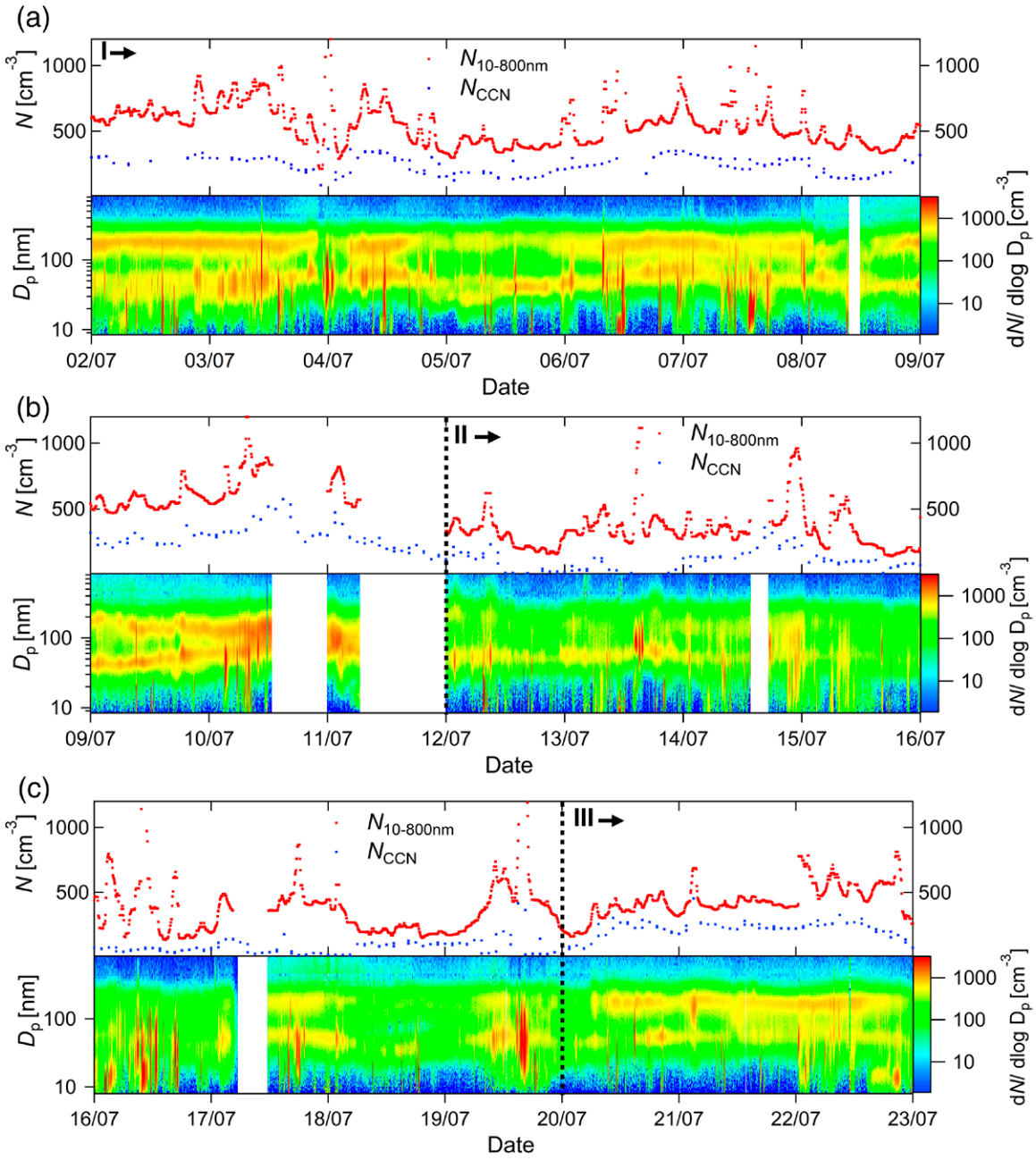

Fig. 7. Time series of particle number concentration from 10 to 800 nm ($N_{10–800nm}$), number concentration of CCN measured at 0.2% supersaturation (N_{CCN}), and particle number size distribution over the measurement period from 2 until 23 Jul 2017 at ENA. The labels I, II, and III and the dashed black lines indicate the starts of the three synoptic periods of the ACORES campaign. White areas represent periods without valid data.

±100 m around cloud top providing steep profiles into the cloud-top region. For a few flights, additional legs at constant height in the subcloud layer (SCL) were flown in order to estimate particle fluxes.

Selected highlights

The cloudy marine boundary layer: Vertical structure and entrainment interfacial layer (9 July 2017 case study). The general—often complex—structure in terms of temperature, moisture, and aerosol stratification of the cloudy MBL and the FT is undersampled in the area of the eastern North Atlantic. To obtain high-resolution data of the vertical structure of the MBL and their link to the EIL, specific flights were performed. The flight strategy was based on

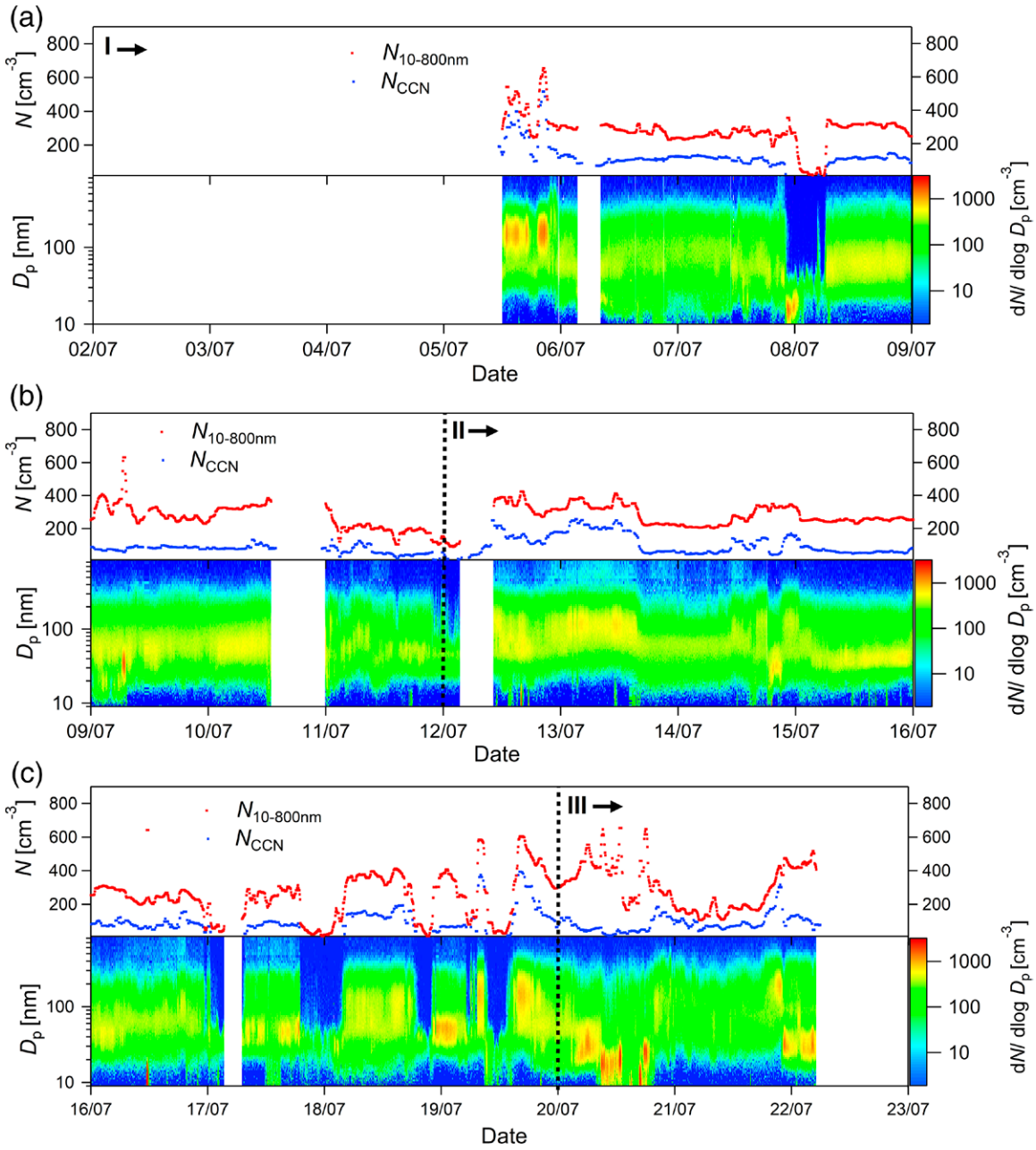

Fig. 8. Time series of particle number concentration from 10 to 800 nm ($N_{10-800nm}$), number concentration of CCN measured at 0.2% supersaturation (N_{CCN}), and particle number size distribution over the measurement period from 2 until 23 Jul 2017 at OMP. The labels I, II, and III and the dashed black lines indicate the starts of the three synoptic periods of the ACORES campaign. White areas represent periods without valid data.

a combination of vertical profiles and level flights at different heights combined with porpoise dives of ±50 m around cloud top.

As an example, on 9 July 2017 a measurement flight started with a vertical profile shortly after take-off revealing a 150-m-thick Sc layer between 1,100 and 1,250 m, as depicted in Figs. 9a–d. This flight was performed offshore north of Graciosa with a maximum distance to the island of about 15 km. Observations above 200 m are considered to be unaffected by the island and representative of the undisturbed eastern North Atlantic. The Sc layer as observed during the first profile is characterized by comparably low LWC with maximum values around 0.2 g m^{-3} and droplet number concentrations $N_d \approx 200$ cm^{-3} (Fig. 9b). The profile of the radiation induced temperature tendency ζ_{ter} was estimated from the vertical radiative flux

Table 5. Overview of all flight times and conditions.

Period	No.	Date	Start (UTC)	End (UTC)	Conditions and comments
1	1	3 Jul 2017	1424	1608	Test flight
	2	4 Jul 2017	1304	1503	Rain before take-off, afterward only thin Sc
	3	5 Jul 2017	1418	1609	High variability in aerosol around inversion
	4	7 Jul 2017	1030	1231	Dissipating Sc over ocean; isolated convective Cu close to island
	5	8 Jul 2017	1428	1626	Thick low Sc with strong capping inversion
	6	9 Jul 2017	0934	1125	Sc with strong capping inversion, many porpoise dives, "golden day"
	7	10 Jul 2017	1050	1251	Sharp inversion with only few Cu hum, higher N_p in MBL compared to FT
2	8	13 Jul 2017	1355	1523	Sc below sharp inversion; high N_p in FT
	9	14 Jul 2017	1327	1530	Sc with capping inversion, N_p peaks around inversion
	10	15 Jul 2017	1446	1614	Several St/Sc layers and few Cu below moderate inversion; rain showers
	11	16 Jul 2017	0941	1144	Sc below weak inversion, second strong inversion; low N_p in MBL, high N_p in FT, "golden day"
	12	16 Jul 2017	1412	1554	Few Cu below Sc layer capped by strong inversion with high N_p above, drizzle
	13	17 Jul 2017	1351	1603	Variable cloud conditions without clear inversion, strong wind
	14	18 Jul 2017	1501	1704	Quite homogeneous Sc, many porpoise dives, two different aerosol layers in FT
3	15	21 Jul 2017	0945	1158	Sc with high LWC, N_p peaks in Sc
	16	21 Jul 2017	1357	1609	Thin, dissipating Sc with second thicker Sc layer above
	17	22 Jul 2017	1244	1454	Almost cloudless at the beginning with strong inversion, later on Sc in lee of island

divergence obtained by the terrestrial irradiance observations on ACTOS and SMART-HELIOS following the method by Egerer et al. (2019). The minimum values of ζ_{ter} are on the order of –12 K h^{-1} and are located close to the cloud top representing the cloud-top cooling, which is a major source for negatively buoyant cloud parcels and, therefore, a driver for cloud-top entrainment. The cloud top is characterized by a sharp inversion with an increase in Θ by ~6 K over a height of 40 m (e.g., the space between the green and red box in Fig. 9c) and a decrease in water vapor density ρ_v of 5 g m^{-3} over the same height range. It is worth mentioning that above the inversion, humidity increases again with height indicating advection of humid air masses in the FT.

The horizontal wind speed (Fig. 9d) shows some shear at cloud top with increasing wind speed from 3.5 to 5.3 m s^{-1}. Even stronger shear has been observed during other days. The balance between wind shear as a major driver of turbulence and the typical stable stratification in the cloud-top region is one of the most important problems in terms of cloud-top entrainment. Based on previous work by Katzwinkel et al. (2012), Malinowski et al. (2013), this topic will be investigated in further studies, in conjunction with the role of radiative cooling at cloud top.

The aerosol particle number concentration N_p is of order 480 cm^{-3} below the cloud layer with negligible vertical variation and 290 cm^{-3} inside the cloud and in the FT. The difference of about 210 cm^{-3} agrees remarkably well with the maximum of N_d indicating the number of activated aerosol particles. The N_{CCN} (measured at 0.2% supersaturation) shows a quite similar structure compared to N_p although the respective values are factor 2 smaller.

The lower part of Fig. 9 shows median aerosol number size distributions measured in the MBL, in the cloud, and in the FT. Measurements from OMP during the flight agree well with those from the FT, indicating that aerosol properties are homogeneous over the whole region on that day. Similarly, measurements from ENA agree well with those in the MBL showing that ENA represents the MBL in this case. The number size distribution in the MBL is characterized by

a bimodal shape consisting of Aitken and accumulation mode. The latter one disappeared inside the cloud layer due to activation and only the Aitken mode is visible. The FT exhibits also only one single mode with a mean diameter 50 nm and a significantly lower number concentration.

Figure 10 shows a 26-min-long portion of porpoise dives between 1,100 and 1,350 m above sea level as observed on 9 July 2017. The upper panel includes the sonic temperature T_s, estimated cloud top, and altitude. The lower panel of Fig. 10 shows the interstitial aerosol particle concentration and the LWC indicating the cloud portion. The green shaded areas indicate parts with aerosol bursts with peak concentrations of up to 6,000 cm^{-3} which are out of scale. These aerosol bursts are most probably caused by nucleation, a process that has been observed quite frequently at cloud edges (Keil and Wendisch 2001; Wehner et al. 2015). The top-right panel shows probability density functions (PDFs) of droplet sizes as observed during the last ascent. A clear tendency to larger droplets with peak diameters around 18–20 μm around cloud top is observed.

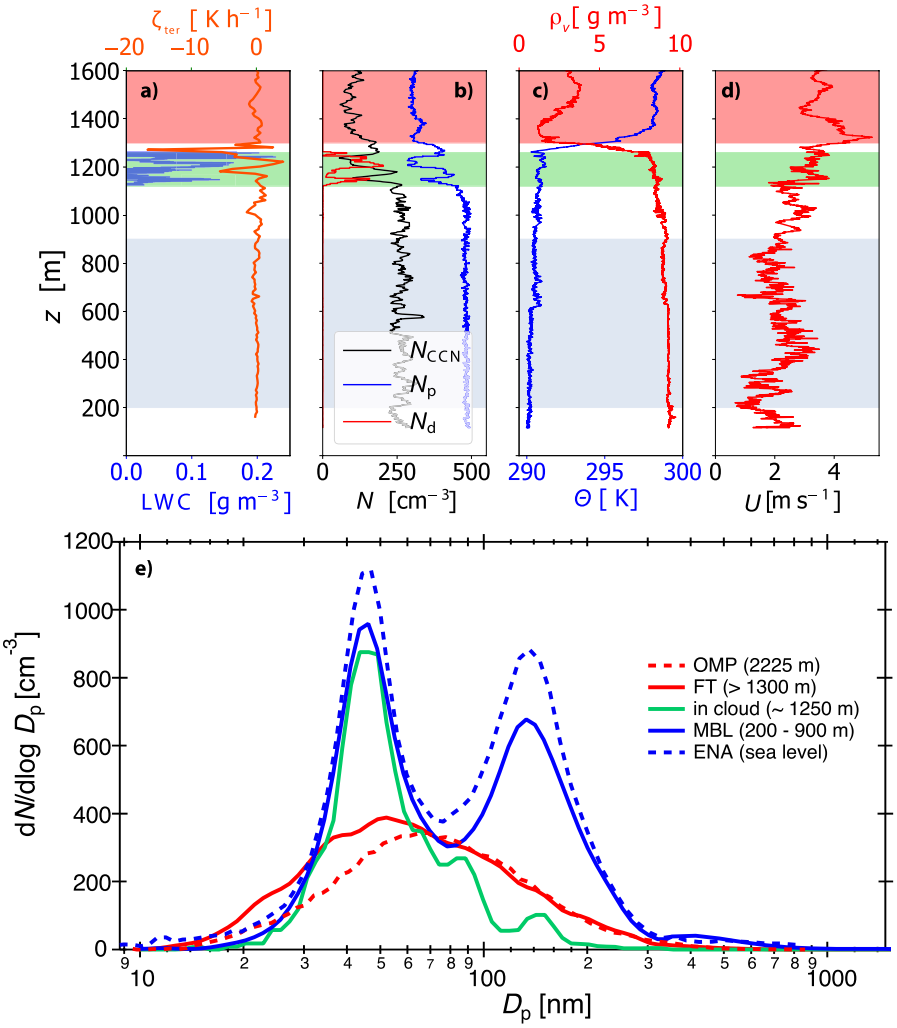

Fig. 9. Vertical profiles of (a) LWC and temperature tendency (ζ_{ter}); (b) number concentration of aerosol particles (N_p), droplets (N_d), and CCN (N_{CCN} at 0.2% supersaturation); (c) water vapor density (ρ_v) and potential temperature (Θ); and (d) horizontal wind velocity (U) measured on 9 Jul. The colored areas refer to the height intervals for which (e) median particle number size distributions are shown for MBL, in cloud, and FT and on ground-based sites. The blue-shaded area in (a)–(d) marks the MBL (200 < z < 900 m), the red area marks the FT (z > 1,300 m) and the green area marks the cloud region. The dotted lines marks the size distributions measured at the ENA and OMP during the ACTOS flight.

One particular problem on cloud-top entrainment concerns the spatial homogeneity of this process. It is well-known that the mixing depends on several factors, such as the strength of the inversion, but also on wind shear, which can promote vertical mixing. Figure 11 shows two selected vertical profiles from the same flight as presented in Fig. 10. The left profiles were observed during the second ascent in Fig. 10, whereas the right profile was measured during the last descent in Fig. 10. For both cases, the difference in T_s over the whole inversion is about 3 K. However, the inversion depth of the right profile is about half compared to the left profile resulting in 2-times-stronger gradients of T_s and ρ_v. The two different profiles illustrate the spatial variability of cloud-top structure within one single Sc cloud deck with highly variable inversion strength and wind shear resulting in high spatial variability of

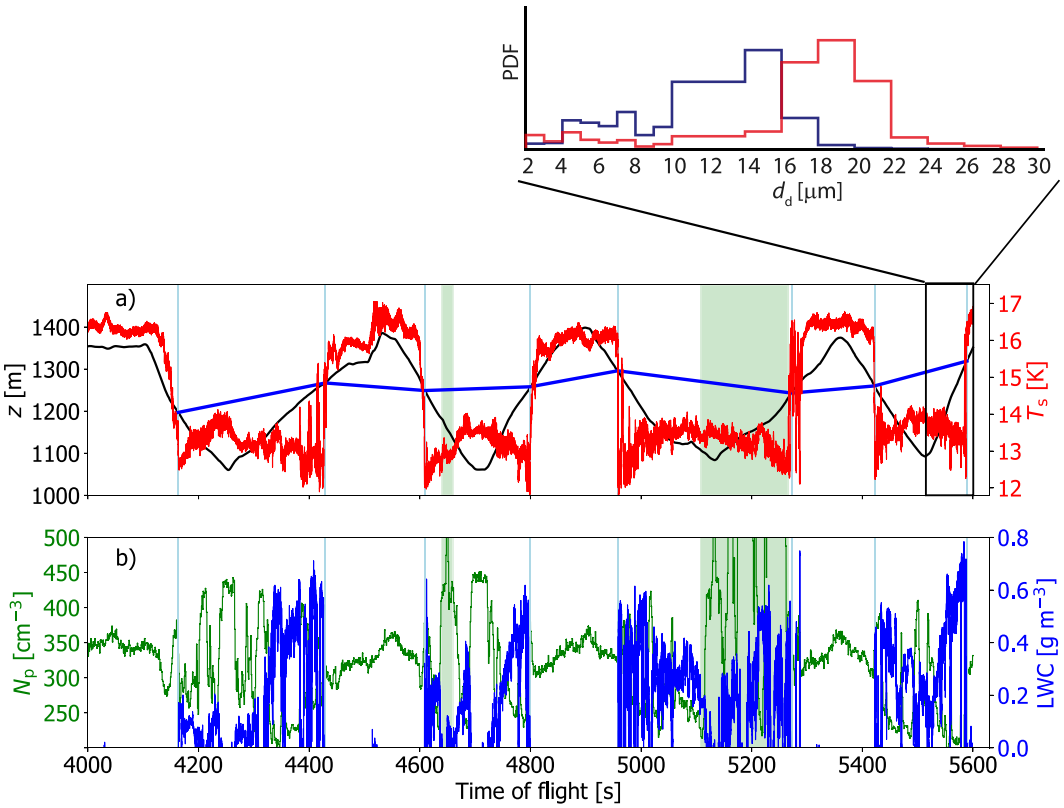

Fig. 10. Time series of (a) measurement height (black line) including estimated cloud top (blue line), fluctuations of the sonic temperature T_s (red line) and (b) of N_p and LWC during a sequence of porpoise flights measured on 9 Jul. Green-shaded periods exhibit several spikes in N_p that are cut in this plot for more detailed presentation. (top right) As an inlay, the probability density functions (PDFs) of the droplet diameter d_d close to cloud top (red curve) and in the lower cloud part (dark blue curve) are shown with arbitrary units. The PDFs are based on observations during the final ascent marked with the black box.

mixing (Katzwinkel et al. 2012). These preliminary findings raise the questions how turbulence properties do vertically vary within the EIL, and how do these depend on different strengths of the temperature inversion and wind shear?

Aerosol stratification under cloudless conditions (5 July 2017 case study). The second case study shows a measurement example under cloudless conditions with a focus on physical aerosol properties and aerosol stratification. This flight was organized in east–west oriented patterns of 12-km length about 2 km north of Graciosa. In the left panel of Fig. 12, the vertical profile as sampled shortly after takeoff is shown. The potential temperature Θ and water vapor density ρ_v indicate a 700-m-thick well-mixed layer (ML) with height-independent aerosol number concentration of N_p = 400 cm^{-3} and N_{CCN} = 130 cm^{-3}, respectively. Above 700 m, the atmosphere is stably stratified up to the maximum height of the profile (2,000 m) with a generally decreasing humidity but several distinguished humidity layers and a pronounced minimum just above the ML. Aerosol number concentrations exhibit higher values above ML, but organized in several well-separated layers including one thin layer at 1,550 m with concentrations even lower compared to the ML. Interestingly, these aerosol layers are not necessarily qualitatively correlated with humid layers. The physical properties of the aerosol population indicate a clear cut between aerosol in the ML and above. Several flight legs at a constant height are used for estimating aerosol particle number size distributions that are shown in the right panel of Fig. 12. The yellow-shaded area shows three particle number size distributions (PNSDs) measured with ACTOS within the

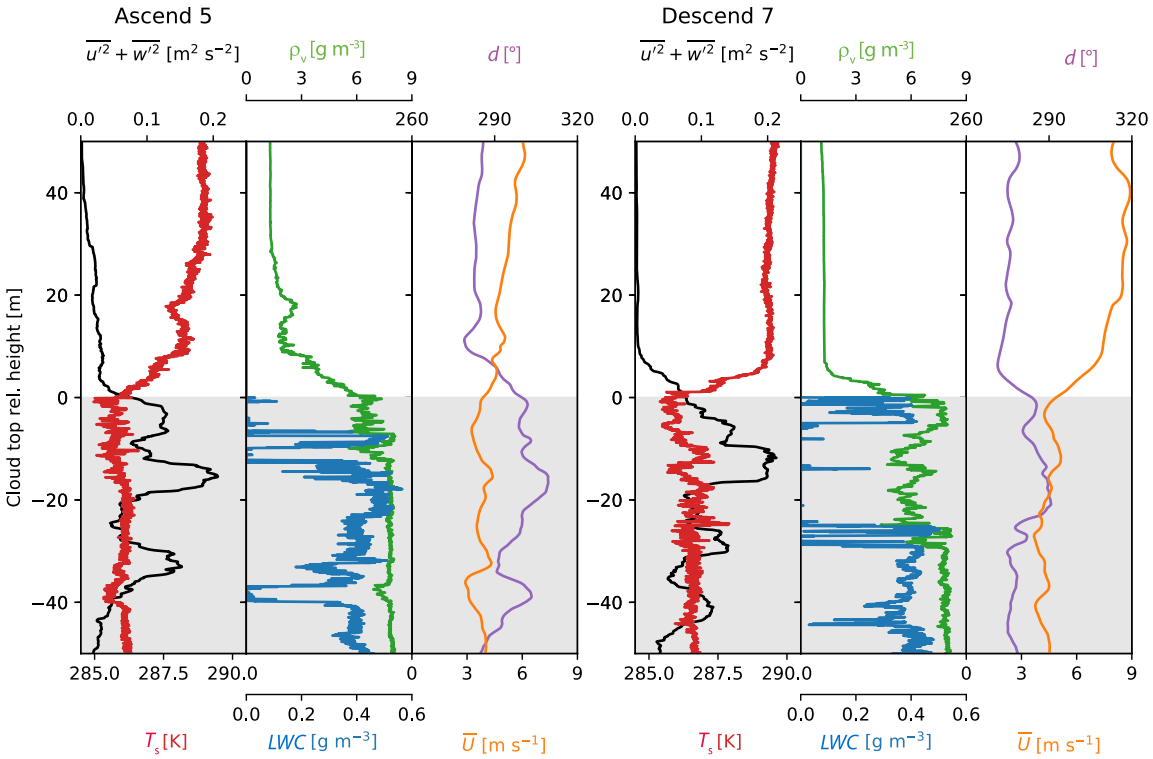

Fig. 11. Vertical profiles taken from (left) an ascent and (right) a descent on 9 Jul 2017. In between the observations of the two profiles 7.5 min passed. For each panel, T_s (red, bottom axis) and $\overline{u'^2} + \overline{w'^2}$ (black, top axis) are depicted in the leftmost plot. The center plot shows LWC (blue, bottom axis) and ρ_v (green, top axis). The right plot depicts $\overline{U}$ (orange, bottom axis) and the wind direction (purple, top axis). The cloud-top relative height is chosen such that 0 m represents the cloud top. The extend of both profiles is set to ±50 m relative to cloud top. The gray background marks the cloud.

ML, being characterized by two clearly separated modes: one Aitken mode with a peak at 50 nm and an accumulation mode with a peak at 200 nm. These PNSDs observed at 120, 430, and 560 m by ACTOS compare qualitatively well with the distribution observed at the ENA site. This is worth mentioning because the ACTOS distributions are based on the average over three to five scans of about 2 min each whereas the ENA and OMP distributions are averaged over the entire ACTOS flight of about 2 h, which results in much more robust statistics. The top-right panel of Fig. 12 shows the distributions observed at 1,600 and 2,000-m height, respectively—all well above the ML. These distributions show a significant accumulation mode with a peak slightly shifted to diameters below 200 nm compared to the ML observations but without a pronounced Aitken mode. Only a small shoulder around 60 nm is visible for both distributions. Interestingly, this shoulder is most obvious for the leg at 1,600 m in the region with the minimum in total aerosol number concentration. In addition to the two distributions based on ACTOS observations, the data from OMP at 2,225 m are shown. Qualitatively, this distribution also compares well with the ACTOS observations for comparable heights and shows the same accumulation mode and small shoulder around 60 nm for an Aitken mode. This agreement suggests again that the OMP data are representative of the aerosols well above the ML for the overall region and with little local surface influence confirming previous findings based on trace gases and modeling (e.g., Kleissl et al. 2007; Collaud Coen et al. 2018). The complex aerosol stratification is different to previous observations (e.g., Collins et al. 2000) in the eastern North Atlantic. Based on the profiles shown in Fig. 12 a well-mixed layer up to about 700 m is obvious. It is topped by a strong temperature inversion and a clear hydrolapse but combined with an increase of aerosol concentration. The aerosol stratification above this inversion is

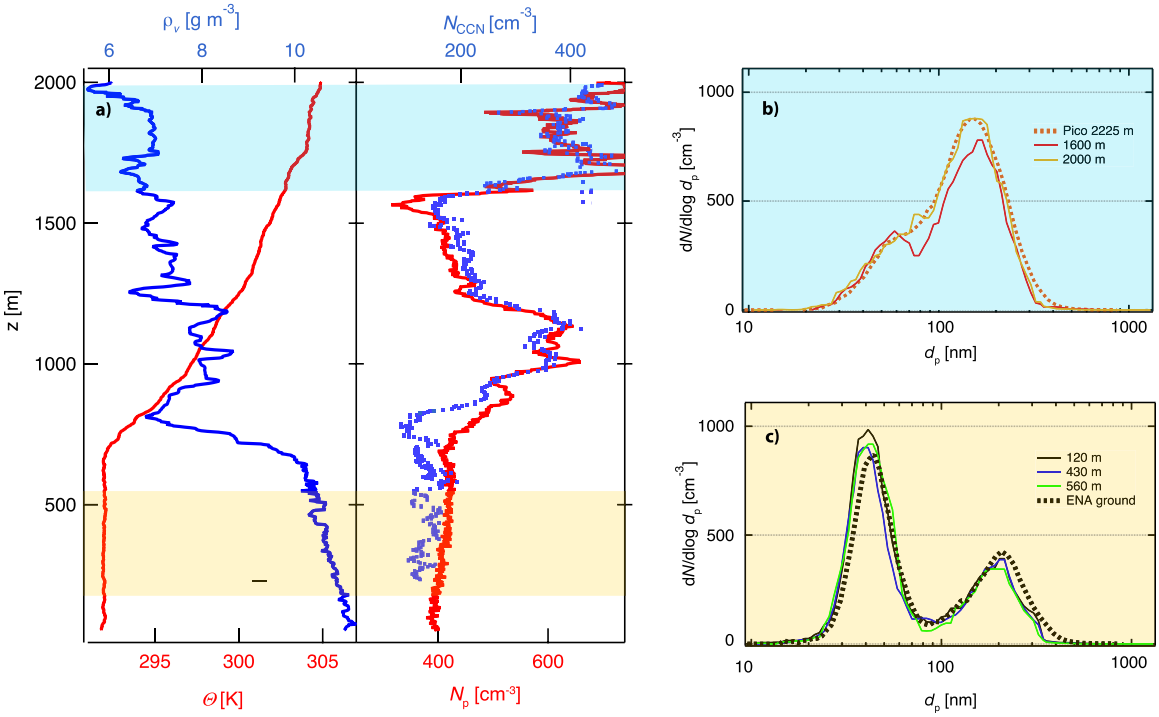

Fig. 12. (a) A vertical profile of Θ (red line), ρ_v (blue line), N_{CCN} measured at 0.2% supersaturation (blue dots), and N_p (red line) as observed during a cloudless day on 5 Jul 2017. (b),(c) Aerosol particle size distributions as observed by ACTOS in different heights. The background color indicates the height region in the corresponding profile of (a). Additionally, ground-based size distributions at the ENA site (at sea level) and at OMP in 2,225-m height are added.

comparable complex and it turns out that general aerosol stratification under cloudy and cloudless conditions will become one of the major topics of the ACORES project.

Horizontal variability of cloud-top temperature (21 July 2017 case study). Brightness temperatures T_b of the cloud top are measured with an infrared camera. Figure 13b shows a two-dimensional field of T_b obtained above an inhomogeneous Sc observed on 21 July 2017. For this example, SMART-HELIOS was located about 790 m above cloud top providing a wide view on the cloud field by covering an area of 610 m × 460 m. The Sc shows a range of T_B between 11° and 20°C. The PDF of T_b is shown in Fig. 13c for the entire image. Large areas of the image are dominated by low brightness temperatures corresponding to the top of the Sc. In these areas, the horizontal variability is low indicating that the cloud-top altitude is rather constant, limited by the temperature inversion. A second mode of high temperatures of about 19.5°C indicates cloudless areas, where the emission of terrestrial radiation by the warm sea surface dominates the measured T_b. Values of T_b between these two modes characterize optically thinner parts of the stratocumulus. With decreasing optical thickness, these areas become more transmissive for the radiation emitted by the surface. These optically thinner areas are typically narrow and deviate strongly from T_b of the opaque cloud parts, which leads to a positive skewness of the PDF (Hogan et al. 2009; Ghate et al. 2014). These measurements show that T_b can significantly change on horizontal scales of less than 100 m and cloud-top cooling is highly variable in space and time. As Jakub and Mayer (2017) suggest, such a horizontal variability of radiative processes need to be considered to understand the interaction of radiative and dynamic processes in Sc.

Small-scale features of the temperature inversion above an Sc deck (9 July 2017 case study). Prior work has shown that the EIL above the STBL extends typically a few tens of

meters in the vertical (Haman et al. 2007; Malinowski et al. 2013), with anisotropic, flat turbulent eddies, sometimes as thin as a few tens of centimeters (Katzwinkel et al. 2012; Jen-La Plante et al. 2016). High-resolution, collocated instruments, the moderate TAS of ACTOS, and the adopted flight patterns allowed investigating these features with unprecedented detail. High-frequency velocity measurements were used to document the changing character of turbulence and the variability of mixing processes across the sublayers of the entrainment zone (Katzwinkel et al. 2012; Malinowski et al. 2013; Jen-La Plante et al. 2016). Temperature fluctuations from the very high response UFT were exploited to zoom in on the eddy structure in the initial phases of mixing.

Figure 14 shows just one particularly interesting example of thermodynamic, turbulence, and microphysical properties observed during a cloud-top penetration recorded during the flight on 9 July. It is a rare example of an extremely thin and sharp (~4 K over a vertical distance of ~0.8 m) inversion right above the cloud top. Within the inversion layer, very narrow, sometimes few-centimeters-thick filaments with temperature contrasts up to 2 K can be noticed (relative distance 116–122 m in the bottom panel of Fig. 14). Such structures, with well-defined filaments of remarkable temperature differences, might correspond to developing Kelvin–Helmholtz vortices. Typically, they appear at the shear interfaces separating different stably stratified layers of the atmosphere. Air patches engulf from one layer into another and then mix further until the viscosity reduces gradients at small scale. One-dimensional cross section through the resulting vortices would include jumps of the amplitude up to the difference between the values in the lower and the upper layer. For Sc and the FT, such fluctuations are observed for both temperature and humidity.

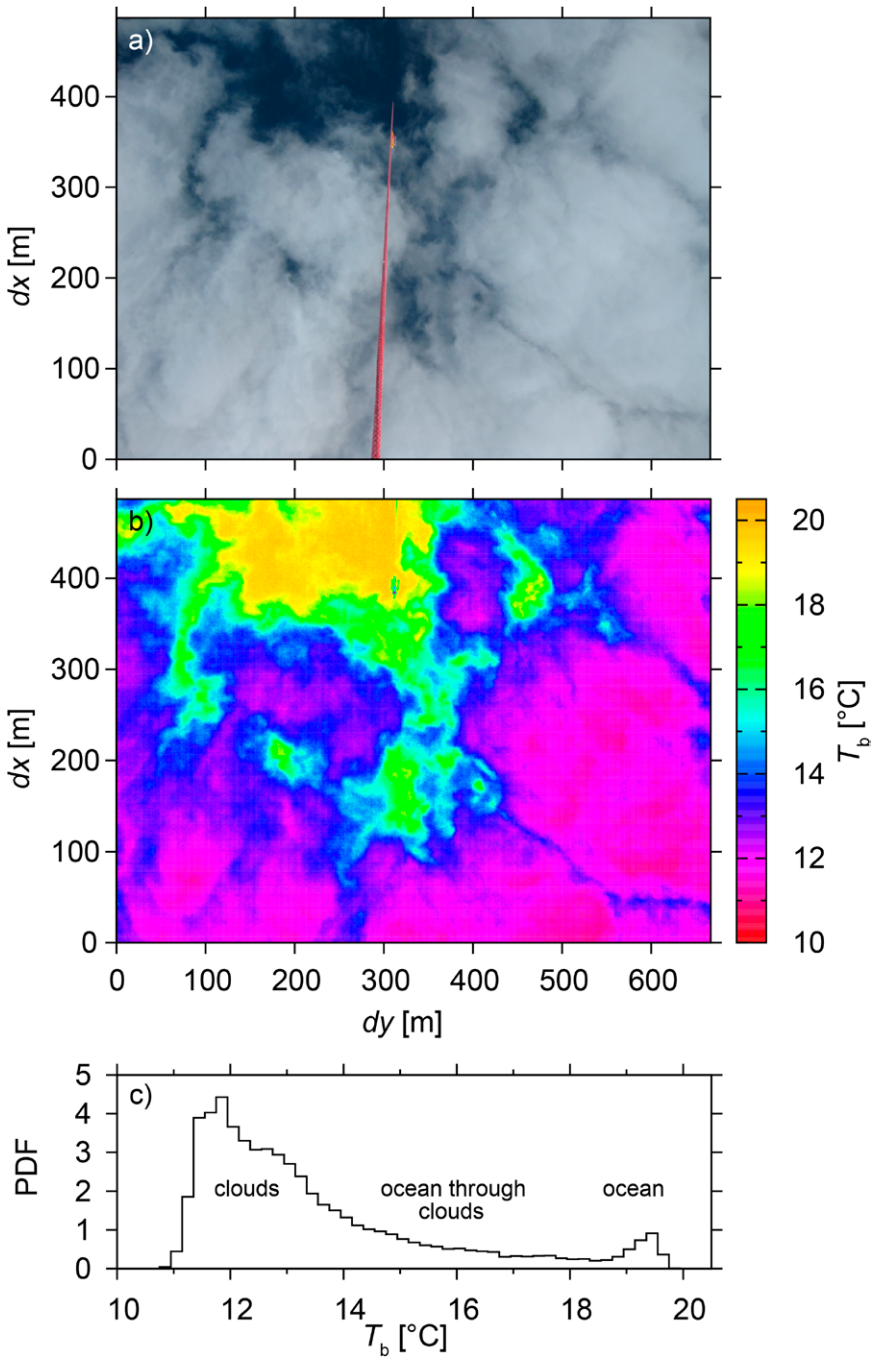

Fig. 13. (a) Image of the cloud in the visible wavelength range taken from above the cloud looking in nadir direction. (b) Infrared image from the GOBI camera for the same image section. (c) Corresponding PDF of the brightness temperature, showing two maxima for cloud and ocean temperatures and a broad transition zone between both maxima where the ocean is visible through the clouds.

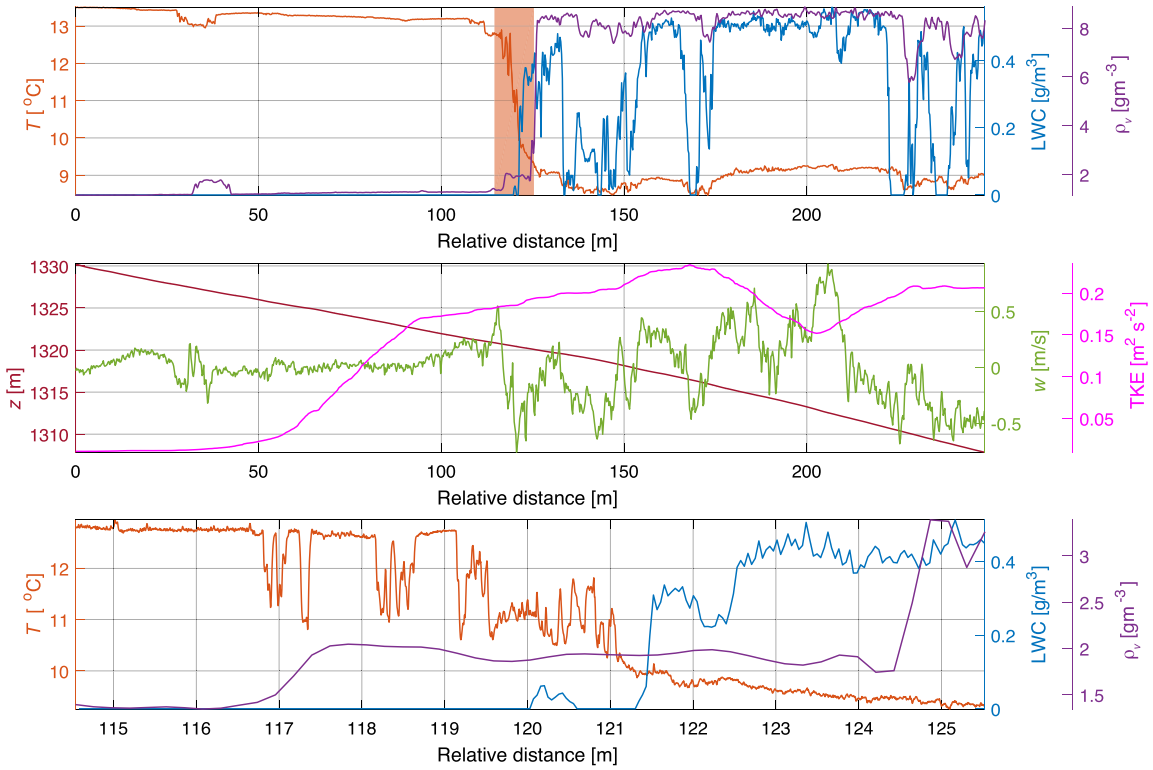

Fig. 14. Observation of direct FT–MBL mixing across the sharp single-layer inversion performed with ACTOS during descent from the FT into the cloud. Measurements are presented with respect to the relative distance covered in the horizontal direction. (top) Temperature (UFT), water vapor density (LICOR), and liquid water content (PVM-100 A). (middle) Vertical wind speed and turbulent kinetic energy (sonic), as well as the ACTOS altitude in the course of the descent. TKE was derived from longitudinal and vertical wind fluctuations by Reynolds decomposition with 10-s averaging. (bottom) An enlarged portion of the penetration, in order to show the fine structure in the cloud-top region (indicated by the red shaded region in the top panel).

The second half of the segment shown in Fig. 14 (relative distance 120–125 m) shows that the amplitude of temperature fluctuation decreases with height. The decreasing mean temperature and increasing LWC reflect the mixing of cloud-top air with air from the inversion. Resolution of the LWC probe does not allow for verification whether filaments of LWC can be as narrow as those of temperature in the dry region above. However, the nearly constant water vapor density between 117- and 124-m relative distance, which is reduced with respect to the high in-cloud value, suggest that this penetration captured a transient mixing event with ongoing evaporation.

Comparison of ACTOS in situ cloud turbulence observations with remote radar observations (16 July 2017 case study). The close proximity of the helicopter flights to the ENA site allows for near-direct comparison of cloud-turbulence properties derived from in situ ACTOS measurements and retrieved from remote sensing data. For the purposes of this paper, we use turbulence kinetic energy dissipation rate ε for the comparison. The dissipation rate is of fundamental importance, not only to turbulence energy budgets, but also to cloud processes such as scalar mixing and droplet collision rates (Shaw 2003; Wyngaard 2010). Comparisons between in situ and remotely derived dissipation rates are rare, with a notable exception being the study of Shupe et al. (2012) in which measurements in Arctic stratocumulus clouds from a tethersonde were compared to retrievals from a Doppler cloud radar. They found root-mean-square differences of factors of 4–6, which decreased to 2–3 when spatial sampling lags were taken into account. In this paper we make a comparison

of dissipation rates measured near the top of a stratocumulus cloud deck during one flight in which the wind speed was directed from the flight location toward the ENA site. A more complete study will be published separately.

The comparison shown here is from the 16 July flight, and takes data from the region of the flight path highlighted in Fig. 15. The dissipation rate is obtained from the ACTOS sonic anemometer measurement of the vertical velocity component, recorded at 100 Hz. The second-order longitudinal velocity structure function is calculated from the velocity time series by considering 1-s samples. In log–log coordinates, a line with slope +2/3 is fitted to the inertial range of the structure function, and the intercept allows the dissipation rate to be estimated (Siebert et al. 2010). The resulting histogram of ε values is shown in Fig. 15. Dissipation rate is also estimated from the second-generation Ka-band ARM zenith-pointing radar (KAZR2; Kollias et al. 2016; Lamer et al. 2019) through 0.5-Hz sampling of the KAZR mean Doppler velocity. The dissipation rate is estimated by considering power spectra with inertial range slopes near −5/3 and using standard Kolmogorov scaling (Borque et al. 2016). Each value is based on a 600-point sample. The upper insert in Fig. 15 shows the vertical profile of ε

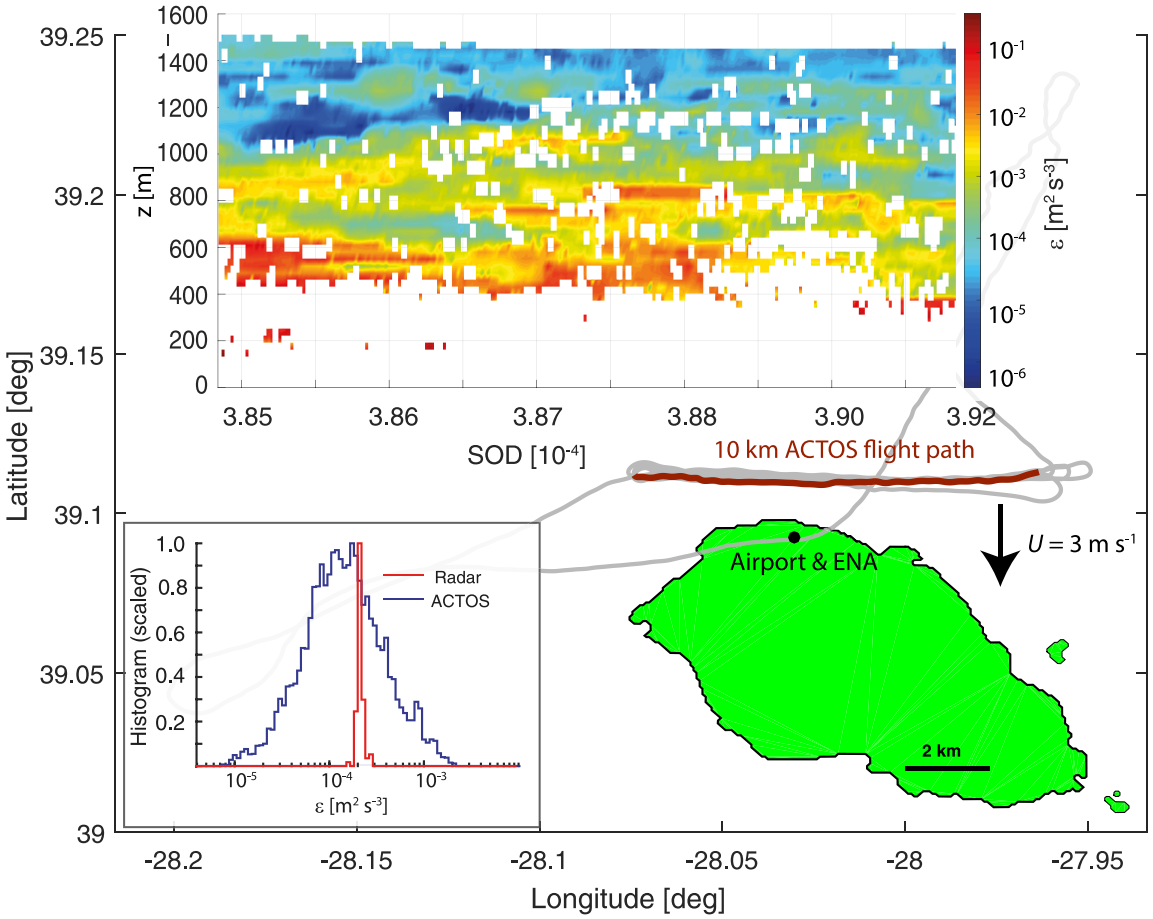

Fig. 15. Turbulence energy dissipation rates in stratocumulus clouds: the ACTOS flight path for the flight on 16 Jul is shown, emphasizing its proximity to the ENA site, as well as the favorable wind conditions for comparison without significant island effects. The highlighted part was flown in a stratocumulus layer at a mean height of 1,460 m. The mean wind was from the north with $U = 3$ m s^{-1}. (top inset) A time series of the vertical profile of ε (time given in seconds of day). Significant variability in ε is observed, so only the cloud-top measurements were used in the comparison. (bottom-left inset) The derived turbulence kinetic energy dissipation rates from the in situ ACTOS measurements (blue histogram) and the ENA radar measurements (red histogram). The histograms have been scaled to have equal peak height for ease of comparison. The mean dissipation observed by ACTOS is $\bar{\varepsilon} = 2.1 \times 10^{-4}$ m^2 s^{-3} with $\sigma_\varepsilon = 2.4 \times 10^{-4}$ m^2 s^{-3} and $\bar{\varepsilon} = 2.0 \times 10^{-4}$ m^2 s^{-3} with $\sigma_\varepsilon = 1.8 \times 10^{-5}$ m^2 s^{-3} as observed by radar.

versus time as derived from the radar measurements. There is substantial vertical variability in ε, so it is important to take values consistent with the ACTOS flight level. We have used radar samples from the 1,480-m level, which is the highest cloud level recorded during the corresponding ACTOS sampling time. For comparison, the ACTOS sampling had an average altitude of approximately 1,460 m. The resulting histogram of ε from the radar is shown in Fig. 15. Note that the histograms have been scaled so that their peak heights are the same; this is to facilitate comparison even when the widths differ greatly. The mean ε estimated from the ACTOS measurements is $\bar{\varepsilon} = 2.1 \times 10^{-4}$ m^2 s^{-3}, and from the radar measurements is $\bar{\varepsilon} = 2.0 \times 10^{-4}$ m^2 s^{-3}. This level of agreement seems remarkable, given that even different methods for estimating the dissipation rate from the same time series can result in variability of up to a factor of 2. Whether the agreement is fortuitous will require a dedicated study considering additional flights. The agreement is less accurate when considering the standard deviations of dissipation rate: ACTOS measurements give an estimate of $\sigma_\varepsilon = 2.4 \times 10^{-4}$ m^2 s^{-3} and radar measurements give an estimate of $\sigma_\varepsilon = 1.8 \times 10^{-5}$ m^2 s^{-3}. At least in part, this can be attributed to different averaging times and sample volumes: the vertical radar resolution is 30 m, and the averaging time is 20 min, compared to the ACTOS sample which is essentially spatially localized, with a vertical extent ~20 cm and an averaging time of 1 s that corresponds to 15–20 m for typical flight speeds. Thus, the ACTOS measurements display the variability in ε expected within the inertial range, while the radar provides a narrow distribution expected when the averaging time is much greater than the large-eddy correlation time.

Summary and conclusions

Ground-based aerosol observations, continuously performed at two measurement stations to sample the MBL and FT during the 1-month period of the ACORES campaign, were combined with high-resolution helicopter-borne measurements of aerosol, cloud, turbulence, and radiation properties collected during 16 flights around Graciosa/Azores. This multilevel and multiscale approach has been exploited to investigate small-scale entrainment processes under cloudy and cloudless conditions with respect to the boundary layer and aerosol stratification.

The helicopter-borne observations suggest that both ground-based stations, although not located at the same island, are representative for the general regional marine environment. In terms of aerosol characteristics, the ENA site represents a larger area of the lower MBL, and the OMP measurements are representative of the FT.

Preliminary data analysis suggests that MBL and FT are disconnected in terms of aerosol properties. The MBL is dominated by bimodal size distributions, while in the FT monomodal size distributions are dominant. Rémillard et al. (2012) pointed out that the subcloud layer in the region of the eastern North Atlantic is often decoupled from the surface layer, which was mostly confirmed during the ACORES campaign. However, this decoupling becomes more obvious from moisture and aerosol changes compared to temperature changes.

New particle formation has been observed in the FT and directly above Sc. To which extent this particle production will influence the aerosol budget, will be part of further analysis. The number of available CCN is in accordance with the shape of the aerosol size distribution. Particles larger than 80 nm served as CCN at a supersaturation 0.2% at all sites. This means that the accumulation mode aerosol particles inhibited the typical hygroscopicity of marine aerosol particles. The observed cases of new particle formation do not influence the number of CCN at typical Sc supersaturation, as they did not grow into the relevant size range within the observation period.

The close collocation of the in situ cloud turbulence and microphysical observations performed by ACTOS with the remote sensing observations of radiation and brightness temperature collected by SMART-HELIOS turned out to be of major importance to verify remote sensing retrievals. In addition, the interpretation of the high-resolution in situ observations

along the flight path requires the combination with the "bird's-eye view" of the cloud field provided by SMART-HELIOS. For the fast transition between cloud and cloudless conditions as observed during ACORES, this key advantage cannot be realized by a single research aircraft. Preliminary analysis indicates that spatial inhomogeneity of brightness temperature varies on scales of less than 100 m significantly. These findings are supported by observed high spatial variability of the turbulent cloud-top structure on similar horizontal scales. Within the same Sc-layer regions with extreme local temperature gradients of up to 4 K m^{-1} were found followed by much smoother vertical gradients of temperature and wind speed in the direct vicinity.

Due to the comparably limited operational area of the helicopter, all airborne observations are located in the vicinity of the ENA site with its comprehensive set of remote sensing devices. In particular, the ACTOS and SMART-HELIOS observations to the north of Graciosa cover the same cloud layers as seen by the remote sensing station, which allows for statistical comparison of cloud and turbulence properties with high fidelity. Energy dissipation rates derived in situ and remotely around cloud top agree remarkably well in terms of their mean values although exhibiting different variability due different averaging.

Finally, the utility of the data are further amplified by its coordination with the Aerosol and Cloud Experiments in the Eastern North Atlantic (ACE-ENA), for which the first project part (IOP1) overlapped in time. The in situ measurements from the ARM Gulfstream G1 aircraft located on Terceira Island, and which also flew in the vicinity of Graciosa, will provide additional opportunities for intercomparison and for combining complementary measurements.

Acknowledgments. This project was supported by several grants of the Deutsche Forschungsgesellschaft (DFG; with Grants SI 1543/4-1, WE 1900/33-1, WE 2757/2-1, and HE 6770/2-1). The campaign was hosted by SATA Air Açores, which is highly appreciated. In particular, we would like to acknowledge Rui Medeiros and Maria Manuela Santos (both SATA) for their support of our stay at Graciosa airport. For the helicopter operation we thank the two pilots Alwin Vollmer and Jürgen Schütz and Georgios Kipros from the rotorflug GmbH, Germany. Technical support was provided by Dieter Schell (enviscope GmbH, Germany) and Astrid Hofmann (TROPOS workshop). The Michigan Tech group acknowledges support from U.S. Department of Energy Office of Science Award DE-SC0020053. The University of Warsaw group acknowledges support from the Polish National Science Centre (Grant Agreement 2013/08/A/ST10/00291). Ed Luke and Pavlos Kollias were supported by the U.S. Department of Energy (DOE) under Contract DE-SC0012704. Data were obtained from and our research was supported by the Atmospheric Radiation Measurement (ARM) User Facility, a U.S. Department of Energy (DOE) Office of Science user facility managed by the Office of Biological and Environmental Research. Stefano Viviani is acknowledged for substantial support of the Mount Pico observations.

Data availability statement. All data from the ACORES study are available from the authors on request. There is a plan to archive the final dataset on the PANGEA server for public access.

References

Albrecht, B. A., C. S. Bretherton, D. Johnson, W. H. Scubert, and A. S. Frisch, 1995: The Atlantic Stratocumulus Transition Experiment—ASTEX. *Bull. Amer. Meteor. Soc.*, **76**, 889–904, https://doi.org/10.1175/1520-0477(1995)076<0889:TASTE>2.0.CO;2.

Andreas, E. L., K. J. Claffy, and A. P. Makshtas, 2000: Low-level atmospheric jets and inversions over the western Weddell Sea. *Bound.-Layer Meteor.*, **97**, 459–486, https://doi.org/10.1023/A:1002793831076.

Bannehr, L., and R. Schwiesow, 1993: A technique to account for the misalignment of pyranometers installed on aircraft. *J. Atmos. Oceanic Technol.*, **10**, 774–777, https://doi.org/10.1175/1520-0426(1993)010<0774:ATTAFT>2.0.CO;2.

Borque, P., E. Luke, and P. Kollias, 2016: On the unified estimation of turbulence eddy dissipation rate using Doppler cloud radars and lidars. *J. Geophys. Res. Atmos.*, **121**, 5972–5989, https://doi.org/10.1002/2015JD024543.

Caughey, S. J., B. A. Crease, and W. T. Roach, 1982: A field study of nocturnal stratocumulus. II: Turbulence structure and entrainment. *Quart. J. Roy. Meteor. Soc.*, **108**, 125–144, https://doi.org/10.1002/qj.49710845508.

China, S., and Coauthors, 2015: Morphology and mixing state of aged soot particles at a remote marine free troposphere site: Implications for optical properties. *Geophys. Res. Lett.*, **42**, 1243–1250, https://doi.org/10.1002/2014GL062404.

——, and Coauthors, 2017: Ice cloud formation potential by free tropospheric particles from long-range transport over the northern Atlantic Ocean. *J. Geophys. Res. Atmos.*, **122**, 3065–3079, https://doi.org/10.1002/2016JD025817.

Collaud Coen, M., and Coauthors, 2018: Identification of topographic features influencing aerosol observations at high altitude stations. *Atmos. Chem. Phys.*, **18**, 12 289–12 313, https://doi.org/10.5194/acp-18-12289-2018.

Collins, D. R., and Coauthors, 2000: In situ aerosol-size distributions and clear-column radiative closure during ACE-2. *Tellus*, **52**, 498–525, https://doi.org/10.3402/TELLUSB.V52i2.16175.

de Roode, S. R., and Q. Wang, 2007: Do stratocumulus clouds detrain? FIRE I data revisited. *Bound.-Layer Meteor.*, **122**, 479–491, https://doi.org/10.1007/s10546-006-9113-1.

Desai, N., S. Glienke, J. Fugal, and R. A. Shaw, 2019: Search for microphysical signatures of stochastic condensation in marine boundary layer clouds using airborne digital holography. *J. Geophys. Res. Atmos.*, **124**, 2739–2752, https://doi.org/10.1029/2018JD029033.

Dong, X., B. Xi, A. Kennedy, P. Minnis, and R. Wood, 2014: A 19-month record of marine aerosol–cloud–radiation properties derived from DOE ARM Mobile Facility deployment at the Azores. Part I: Cloud fraction and single-layered MBL cloud properties. *J. Climate*, **27**, 3665–3682, https://doi.org/10.1175/JCLI-D-13-00553.1.

Dzepina, K., and Coauthors, 2015: Molecular characterization of free tropospheric aerosol collected at the Pico Mountain Observatory: A case study with a long-range transported biomass burning plume. *Atmos. Chem. Phys.*, **15**, 5047–5068, https://doi.org/10.5194/acp-15-5047-2015.

Egerer, U., M. Gottschalk, H. Siebert, A. Ehrlich, and M. Wendisch, 2019: The new BELUGA setup for collocated turbulence and radiation measurements using a tethered balloon: First applications in the cloudy Arctic boundary layer. *Atmos. Meas. Tech.*, **12**, 4019–4038, https://doi.org/10.5194/amt-12-4019-2019.

Ehrlich, A., and M. Wendisch, 2015: Reconstruction of high-resolution time series from slow-response broadband terrestrial irradiance measurements by deconvolution. *Atmos. Meas. Tech.*, **8**, 3671–3684, https://doi.org/10.5194/amt-8-3671-2015.

Gerber, H., B. G. Arends, and A. S. Ackerman, 1994: New microphysics sensor for aircraft use. *Atmos. Res.*, **31**, 235–252, https://doi.org/10.1016/0169-8095(94)90001-9.

——, G. Frick, S. P. Malinowski, J.-L. Brenguier, and F. Burnet, 2005: Holes and entrainment in stratocumulus. *J. Atmos. Sci.*, **62**, 443–459, https://doi.org/10.1175/JAS-3399.1.

——, ——, ——, H. Jonsson, D. Khelif, and S. Krueger, 2013: Entrainment rates and microphysics in post stratocumulus. *J. Geophys. Res. Atmos.*, **118**, 12 094–12 109, https://doi.org/10.1002/jgrd.50878.

——, S. P. Malinowski, and H. Jonsson, 2016: Evaporative and radiative cooling in POST stratocumulus. *J. Atmos. Sci.*, **73**, 3877–3884, https://doi.org/10.1175/JAS-D-16-0023.1.

Ghate, V., B. Albrecht, M. Miller, A. Brewer, and C. Fairall, 2014: Turbulence and radiation in stratocumulus-topped marine boundary layers: A case study from VOCALS-REx. *J. Appl. Meteor. Climatol.*, **53**, 117–135, https://doi.org/10.1175/JAMC-D-12-0225.1.

Haman, K. E., A. Makulski, S. P. Malinowski, and R. Busen, 1997: A new ultrafast thermometer for airborne measurements in clouds. *J. Atmos. Oceanic Technol.*, **14**, 217–227, https://doi.org/10.1175/1520-0426(1997)014<0217:ANUTFA>2.0.CO;2.

——, S. P. Malinowski, M. J. Kurowski, H. Gerber, and J.-L. Brenguier, 2007: Small-scale mixing processes at the top of a marine stratocumulus—A case-study. *Quart. J. Roy. Meteor. Soc.*, **133**, 213–226, https://doi.org/10.1002/qj.5.

Hersbach, H., and Coauthors, 2018a: ERA5 hourly data on pressure levels from 1979 to present. Copernicus Climate Change Service (C3S) Climate Data Store (CDS). Accessed 14 May 2020, https://doi.org/10.24381/cds.bd0915c6.

——, and Coauthors, 2018b: ERA5 hourly data on single levels from 1979 to present. Copernicus Climate Change Service (C3S) Climate Data Store (CDS). Accessed 11 May 2020, https://doi.org/10.24381/cds.adbb2d47.

Hogan, R. J., A. L. M. Grant, A. J. Illingworth, G. N. Pearson, and E. J. O'Connor, 2009: Vertical velocity variance and skewness in clear and cloud-topped boundary layers as revealed by Doppler lidar. *Quart. J. Roy. Meteor. Soc.*, **135**, 635–643, https://doi.org/10.1002/qj.413.

Honrath, R. E., and Coauthors, 2004: Regional and hemispheric impacts of anthropogenic and biomass burning emissions on summertime CO and O_3 in the North Atlantic lower free troposphere. *J. Geophys. Res.*, **109**, D24310, https://doi.org/10.1029/2004JD005147.

Jakub, F., and B. Mayer, 2017: The role of 1-D and 3-D radiative heating in the organization of shallow cumulus convection and the formation of cloud streets. *Atmos. Chem. Phys.*, **17**, 13 317–13 327, https://doi.org/10.5194/acp-17-13317-2017.

Jen-La Plante, I., and Coauthors, 2016: Physics of Stratocumulus Top (POST): Turbulence characteristics. *Atmos. Chem. Phys.*, **16**, 9711–9725, https://doi.org/10.5194/acp-16-9711-2016.

Kahl, J. D., 1990: Characteristics of the low-level temperature inversion along the Alaskan Arctic coast. *Int. J. Climatol.*, **10**, 537–548, https://doi.org/10.1002/joc.3370100509.

Kanitz, T., A. Ansmann, R. Engelmann, and D. Althausen, 2013: North-south cross sections of the vertical aerosol distribution over the Atlantic Ocean from multiwavelength Raman/polarization lidar during Polarstern cruises. *J. Geophys. Res. Atmos.*, **118**, 2643–2655, https://doi.org/10.1002/jgrd.50273.

Katzwinkel, J., H. Siebert, and R. A. Shaw, 2012: Observation of a self-limiting, shear-induced turbulent inversion layer above marine stratocumulus. *Bound.-Layer Meteor.*, **145**, 131–143, https://doi.org/10.1007/s10546-011-9683-4.

Keil, A., and M. Wendisch, 2001: Bursts of Aitken mode and ultrafine particles observed at the top of continental boundary layer clouds. *J. Aerosol Sci.*, **32**, 649–660, https://doi.org/10.1016/S0021-8502(00)00102-6.

Kleissl, J., R. E. Honrath, M. Dziobak, D. Tanner, M. Martin, R. Owen, and D. Helmig, 2007: Occurrence of upslope flows at the Pico mountaintop observatory: A case study of orographic flows on a small, volcanic island. *J. Geophys. Res.*, **112**, D10S35, https://doi.org/10.1029/2006JD007565.

Kollias, P., and Coauthors, 2016: Development and applications of arm millimeter-wavelength cloud radars. *The Atmospheric Radiation Measurement (ARM) Program: The First 20 Years*, *Meteor. Monogr.*, No. 57, Amer. Meteor. Soc., https://doi.org/10.1175/AMSMONOGRAPHS-D-15-0037.1.

Kumala, W., K. E. Haman, M. Kopec, M. K. Khelif, and S. Malinowski, 2013: Ultra-fast thermometer UFTM: High resolution temperature measurements during Physics of Stratocumulus Top (POST). *J. Atmos. Oceanic Technol.*, **6**, 2043–2054, https://doi.org/10.5194/amt-6-2043-2013.

Lamer, K., B. P. Treserras, Z. Zhu, B. Isom, N. Bharadwaj, and P. Kollias, 2019: Characterization of shallow oceanic precipitation using profiling and scanning radar observations at the eastern North Atlantic ARM observatory. *Atmos. Meas. Tech.*, **12**, 4931–4947, https://doi.org/10.5194/amt-12-4931-2019.

Lampert, A., and Coauthors, 2018: Comparison of Lyman-alpha and LI-COR infrared hygrometers for airborne measurement of turbulent fluctuations of water vapour. *Atmos. Meas. Tech.*, **11**, 2523–2536, https://doi.org/10.5194/amt-11-2523-2018.

Lance, C., C. A. Brock, D. Rogers, and J. A. Gordon, 2010: Water droplet calibration of the Cloud Droplet Probe (CDP) and in-flight performance in liquid, ice and mixed-phase clouds during ARCPAC. *Atmos. Meas. Tech.*, **3**, 1683–1706, https://doi.org/10.5194/amt-3-1683-2010.

Lenschow, D. H., and Coauthors, 1988: Dynamics and Chemistry on Marine Stratocumulus (DYCOMS) experiment. *Bull. Amer. Meteor. Soc.*, **69**, 1058–1067, https://doi.org/10.1175/1520-0477(1988)069<1058:DACOMS>2.0.CO;2.

Malinowski, S. P., and Coauthors, 2013: Physics of Stratocumulus Top (POST): Turbulent mixing across capping inversion. *Atmos. Chem. Phys.*, **13**, 12 171–12 186, https://doi.org/10.5194/acp-13-12171-2013.

Mather, J. H., and J. W. Voyles, 2013: The ARM Climate Research Facility: A review of structure and capabilities. *Bull. Amer. Meteor. Soc.*, **94**, 377–392, https://doi.org/10.1175/BAMS-D-11-00218.1.

Rémillard, J., P. Kollias, E. Luke, and R. Wood, 2012: Marine boundary layer cloud observations in the Azores. *J. Climate*, **25**, 7381–7398, https://doi.org/10.1175/JCLI-D-11-00610.1.

Roberts, G. C., and A. Nenes, 2005: A continuous-flow streamwise thermal-gradient CCN chamber for atmospheric measurements. *Aerosol Sci. Technol.*, **39**, 206–221, https://doi.org/10.1080/027868290913988.

Schum, S., B. Zhang, K. Dzepina, P. Fialho, C. Mazzoleni, and L. Mazzoleni, 2018: Molecular and physical characteristics of aerosol at a remote free troposphere site: Implications for atmospheric aging. *Atmos. Chem. Phys.*, **18**, 14 017–14 036, https://doi.org/10.5194/acp-18-14017-2018.

Shaw, R. A., 2003: Particle-turbulence interactions in atmospheric clouds. *Annu. Rev. Fluid Mech.*, **35**, 183–227, https://doi.org/10.1146/annurev.fluid.35.101101.161125.

Shupe, M., I. Brooks, and G. Canut, 2012: Evaluation of turbulent dissipation rate retrievals from Doppler cloud radar. *Atmos. Meas. Tech.*, **5**, 1375–1385, https://doi.org/10.5194/amt-5-1375-2012.

Siebert, H., H. Franke, K. Lehmann, R. Maser, E. W. Saw, D. Schell, R. A. Shaw, and M. Wendisch, 2006: Probing fine-scale dynamics and microphysics of clouds with helicopter-borne measurements. *Bull. Amer. Meteor. Soc.*, **87**, 1727–1738, https://doi.org/10.1175/BAMS-87-12-1727.

——, K. Lehmann, and R. Shaw, 2007: On the use of a hot-wire anemometer for turbulence measurements in clouds. *J. Atmos. Oceanic Technol.*, **24**, 980–993, https://doi.org/10.1175/JTECH2018.1.

——, R. A. Shaw, and Z. Warhaft, 2010: Statistics of small-scale velocity fluctuations and internal intermittency in marine stratocumulus clouds. *J. Atmos. Sci.*, **67**, 262–273, https://doi.org/10.1175/2009JAS3200.1.

Stevens, B., and Coauthors, 2003: Dynamics and Chemistry of Marine Stratocumulus—DYCOMS-II. *Bull. Amer. Meteor. Soc.*, **84**, 579–593, https://doi.org/10.1175/BAMS-84-5-Stevens.

Wang, Q., and B. A. Albrecht, 1994: Observations of cloud-top entrainment in marine stratocumulus clouds. *J. Atmos. Sci.*, **51**, 1530–1547, https://doi.org/10.1175/1520-0469(1994)051<1530:OOCTEI>2.0.CO;2.

Wehner, B., and Coauthors, 2010: Observations of turbulence-induced new particle formation in the residual layer. *Atmos. Chem. Phys.*, **10**, 4319–4330, https://doi.org/10.5194/acp-10-4319-2010.

——, F. Werner, F. Ditas, R. A. Shaw, M. Kulmala, and H. Siebert, 2015: Observations of new particle formation in enhanced UV irradiance zones near cumulus clouds. *Atmos. Chem. Phys.*, **15**, 11 701–11 711, https://doi.org/10.5194/acp-15-11701-2015.

Wendisch, M., and J.-L. Brenguier, Eds., 2013: *Airborne Measurements for Environmental Research: Methods and Instruments*. Wiley-VCH Verlag, 641 pp.

——, T. J. Garrett, and J. W. Strapp, 2002: Wind tunnel tests of the airborne PVM-100A response to large drops. *J. Atmos. Oceanic Technol.*, **19**, 1577–1584, https://doi.org/10.1175/1520-0426(2002)019<1577:WTTOTA>2.0.CO;2.

Werner, F., H. Siebert, P. Pilewskie, T. Schmeissner, R. A. Shaw, and M. Wendisch, 2013: New airborne retrieval approach for trade wind cumulus properties under overlying cirrus. *J. Geophys. Res. Atmos.*, **118**, 3634–3649, https://doi.org/10.1002/jgrd.50334.

——, and Coauthors, 2014: Twomey effect observed from collocated microphysical and remote sensing measurements over shallow cumulus. *J. Geophys. Res. Atmos.*, **119**, 1534–1545, https://doi.org/10.1002/2013JD020131.

Wiedensohler, A., and Coauthors, 2012: Mobility particle size spectrometers: Harmonization of technical standards and data structure to facilitate high quality long-term observations of atmospheric particle number size distributions. *Atmos. Meas. Tech.*, **5**, 657–685, https://doi.org/10.5194/amt-5-657-2012.

Williamson, C. J., and Coauthors, 2019: A large source of cloud condensation nuclei from new particle formation in the tropics. *Nature*, **574**, 399–403, https://doi.org/10.1038/s41586-019-1638-9.

Wood, R., 2012: Stratocumulus clouds. *Mon. Wea. Rev.*, **140**, 2373–2423, https://doi.org/10.1175/MWR-D-11-00121.1.

——, and Coauthors, 2015: Clouds, aerosol, and precipitation in the marine boundary layer: An ARM Mobile Facility deployment. *Bull. Amer. Meteor. Soc.*, **96**, 419–440, https://doi.org/10.1175/BAMS-D-13-00180.1.

Wyngaard, J. C., 2010: *Turbulence in the Atmosphere*. Cambridge University Press, 408 pp.